

JGR Atmospheres

RESEARCH ARTICLE

10.1029/2021JD034528

Key Points:

- Gravity wave (GW) activities in the upper mesosphere over the Antarctic Peninsula are investigated using 14-year meteor radar data
- Orography and jet are the primary wave sources in winter and equinoxes, respectively, and convection is a possible source in autumn/winter
- Ray-tracing of GWs observed from airglow measurements suggests that secondary GWs are mainly generated in winter mesosphere

Supporting Information:

Supporting Information may be found in the online version of this article.

Correspondence to:

H.-Y. Chun,
chunhy@yonsei.ac.kr









Citation:

Song, B.-G., Song, I.-S., Chun, H.-Y., Lee, C., Kam, H., Kim, Y. H., et al. (2021). Activities of small-scale gravity waves in the upper mesosphere observed from meteor radar at King Sejong Station, Antarctica (62.22°S, 58.78°W) and their potential sources. *Journal of Geophysical Research: Atmospheres*, 126, e2021JD034528. <https://doi.org/10.1029/2021JD034528>

Received 1 JAN 2021

Accepted 28 APR 2021

Activities of Small-Scale Gravity Waves in the Upper Mesosphere Observed From Meteor Radar at King Sejong Station, Antarctica (62.22°S, 58.78°W) and Their Potential Sources

B.-G. Song¹ , I.-S. Song² , H.-Y. Chun² , C. Lee¹ , H. Kam³, Y. H. Kim⁴ , M.-J. Kang² , N. P. Hindley⁵ , and N. J. Mitchell^{5,6} 

¹Korea Polar Research Institute, Incheon, South Korea, ²Department of Atmospheric Sciences, Yonsei University, Seoul, South Korea, ³Korea Astronomy and Space Science Institute, Daejeon, South Korea, ⁴Department of Astronomy, Space Science and Geology, Chungnam National University, Daejeon, South Korea, ⁵Centre for Space, Atmospheric and Oceanic Science, University of Bath, Bath, UK, ⁶British Antarctic Survey, Cambridge, UK

Abstract Gravity wave (GW) activities in the upper mesosphere (80–100 km) and their potential sources are investigated using meteor radar observations at King Sejong Station, Antarctica (KSS; 62.22°S, 58.78°W) during recent 14 years (2007–2020). GW activities are estimated by horizontal wind variances of small-scale GWs (periods <2 h, horizontal wavelength <400 km, or vertical wavelength <3–5 km). The wind variances show clear semiannual variations with maxima at solstices, and annual variations are also seen above $z = 90$ km. The deseasonalized wind variances at $z = 96.8$ km have a statistically significant periodicity of ~ 11 years that can be associated with solar cycle variations. Three major potential GW sources in the lower atmosphere are examined. Orography is a potential source of GWs in winter and autumn, when the basic-state wind is westerly from the surface up to the mesosphere. The residual of the nonlinear balance equation (RNBE) at 5 hPa, a diagnostic of the GWs associated with jet stream, is the largest in winter and has a secondary maximum in spring. The correlation between the observed GWs and RNBE is significant in equinoxes, while correlation is low in winter. Deep convection in storm tracks is a potential source in autumn and winter. Secondary GWs generated in the mesosphere can also be observed in the upper mesosphere. Ray-tracing analysis for airglow images observed at KSS indicates that secondary GWs are mostly generated in winter mesosphere, which may be associated with the breaking of orographic GWs.

1. Introduction

Atmospheric gravity waves (GWs) can be generated from various tropospheric sources such as orography, jet stream, and convection, and these waves play a major role in determining the spatiotemporal structure of the middle atmosphere wind and temperature by transferring momentum and energy to high altitudes (Lindzen, 1981). In the mesosphere, GW breaking is frequently observed (Nappo, 2013), and momentum and energy transfer accompanied by GW breaking is essential in accounting for the thermal and wind structure of the mesosphere (Andrews et al., 1987; Fritts & Alexander, 2003; Kim et al., 2003).

Observations of mesospheric GWs have been made using various ground-based instruments: Medium-frequency (MF) and high-frequency radars (Fritts & Vincent, 1987; Vincent, 1984, 1994; Vincent & Fritts, 1987; Vincent & Reid, 1983), lidars (Beatty et al., 1992; Chanin & Hauchecorne, 1981; Lu, Chen, et al., 2015; Lu et al., 2017; Wilson et al., 1991), all-sky airglow imagers (Brown et al., 2004; Fritts et al., 2002), satellites (Ern et al., 2011; Kalisch et al., 2016), and meteor radars (Beldon & Mitchell, 2009; Hocking, 2005; Lee et al., 2013; Liu et al., 2013; Mitchell & Beldon, 2009; Song et al., 2017). Many of these observations have been conducted in high-latitude regions (i.e., the Arctic and Antarctic areas) where mesospheric effects of GWs are significant.

The Southern Hemisphere (SH) high-latitude region around the Antarctic Peninsula is one of the greatest GW activity areas, so-called a *GW hot spot*. Ern et al. (2004) estimated GW momentum fluxes (GWMFs) from temperature perturbations using the Cryogenic Infrared Spectrometers and Telescopes for the Atmosphere (CRISTA) data and showed that their maximum values are observed around Antarctic Peninsula.

Using the High Resolution Dynamics Limb Sounder (HIRDLS) data, Alexander et al. (2008) showed that GWMFs are substantially large at SH high latitudes in May 2006, and the Andes are the primary source of the observed GWs in the mesosphere. Jia et al. (2014) found that GWMFs in the SH stratosphere have large values in high-latitude regions in winter based on the Sounding of the Atmosphere using Broadband Emission Radiometry (SABER) and HIRDLS observations. Hindley et al. (2015) also reported the GW hot spot based on GWMF observations by Global Positioning System radio occultation (GPS-RO). In addition to the satellite observations, Plougonven et al. (2013) showed from super-pressure balloon experiments that GWMFs have local maxima around the Antarctic Peninsula and relatively large values over the southern Andes and Drake Passage. Results from climate models (e.g., Geller et al., 2013), global weather forecast models (e.g., Preusse et al., 2014), and mesoscale models (e.g., Plougonven et al., 2013) have also demonstrated large GWMFs in SH high-latitude regions, especially near the Antarctic Peninsula during winter.

King Sejong Station (KSS), operated by the Korea Polar Research Institute, is located near the Antarctic Peninsula in the GW hot spot areas. Upper mesospheric winds and GW activities at KSS have been observed using a very high frequency (VHF) meteor radar since March 2007 (Lee et al., 2013; Song et al., 2017). Lee et al. (2013) estimated GW activities near the mesopause region during 2007–2009, based on the meteor-variance technique proposed by Mitchell and Beldon (2009) and compared them with the Aura Microwave Limb Sounder (MLS) observations. Song et al. (2017) retrieved low-frequency inertia-GWs (IGWs) during the whole year of 2014 with intrinsic frequencies of $|f| - 3|f|$ where f is the Coriolis parameter, and found that most IGWs propagate in the N-S direction in summer and the NE-SW direction in winter.

Understanding the impacts of GWs in the large-scale circulation in polar regions requires knowledge of GW sources and their propagation processes. Orography has long been considered to be an important GW source in the polar regions. Yoshiki and Sato (2000) showed that GWs in the Arctic stratosphere observed by radiosondes for 10 years (1987–1996) are mainly generated by orography. Plougonven et al. (2008) reported large-amplitude mountain waves over the Antarctic Peninsula from super-pressure balloon observations and mesoscale simulations. Yamashita et al. (2009) showed that orography is the main source of enhanced GWs in winter through the analysis of GW potential energy densities observed with lidar at Rothera station (67.34°S, 68.07°W). Events of intense stratospheric GWs generated by the orography of the Andes and Antarctic Peninsula have also been observed from satellite data (Jiang et al., 2002; Preusse et al., 2002).

The jet stream in the troposphere can be another GW source (Fritts & Nastrom, 1992; Plougonven, 2003; Sato, 1994; Uccellini & Koch, 1987), which has been demonstrated by numerical modeling studies (Kim et al., 2016; O'sullivan & Dunkerton, 1995; Plougonven & Snyder, 2007; Reeder & Griffiths, 1996; Wang & Zhang, 2007; Zhang, 2004). Generation of GWs from the jet stream can be related to the imbalance of the large-scale flow associated with the tropospheric jet stream. In order to diagnose the imbalance, the residual of the nonlinear balance equation (RNBE) has been employed (Hertzog et al., 2001; Moore & Abeling, 1988; Yoo et al., 2020; Zhang et al., 2000, 2001). In addition to tropospheric jets accompanied by frontal systems, the polar night jet in the stratosphere has also been considered to be an important source for GWs. Several observational studies have revealed enhanced GW activities near the stratospheric polar night jet using lidar (Whiteway et al., 1997), radiosonde (Sato & Yoshiki, 2008; Yoo et al., 2020, 2018; Yoshiki et al., 2004; Yoshiki & Sato, 2000), and satellite (Ern et al., 2011; Schroeder et al., 2009; Wu & Zhang, 2004), and strong GW activities have been observed mainly at the edge of the polar vortex (Whiteway et al., 1997; Yoshiki et al., 2004). Given that the edge of the vortex is often located near KSS, the polar night jet in the stratosphere could be an important source of GWs in the upper mesosphere over KSS.

Several studies have demonstrated the importance of convection as a source of GWs in the upper mesosphere. For example, Ern et al. (2011) showed that convective GWs in subtropical monsoon regions can propagate toward mid- and high latitudes in the middle atmosphere and contribute to the summertime wind reversal in the mesosphere using HIRDLS and SABER observations. Some previous studies (e.g., Choi & Chun, 2011, 2013; Kang et al., 2017, 2020; Song & Chun, 2005) have reported that large amplitude cloud top momentum fluxes of convective GWs are often found in winter hemisphere storm track regions (30°–50°N and 30°–50°S). Considering that KSS is located at ~62°S (i.e., the boundary between mid- and high latitudes), deep convection in storm-track regions can be a possible source of GWs observed in the mesosphere at KSS. Choi and Chun (2011) showed that convective GWs transfer westward momentum fluxes poleward as they propagate upward. Choi and Chun (2013) demonstrated that the systematic bias such as excessively

strong SH polar night jet and cold polar temperature in general circulation models (GCMs) can actually be alleviated by including the source-dependent convective GW drag (CGWD) parameterization proposed by Choi and Chun (2011) in the Whole Atmosphere Community Climate Model (WACCM).

Secondary GWs are generated in association with breaking of primary waves due to some tropospheric sources such as orography (Satomura & Sato, 1999; Vadas & Becker, 2018) and convection (Chun & Kim, 2008; Kim & Chun, 2009; Snively & Pasko, 2003). As Heale et al. (2020) categorized, generation of secondary (or called nonprimary) GWs can be accounted for by the GW packet-scale body force mechanism (Vadas et al., 2003, 2018) or the nonlinear cascading mechanism (Bacmeister & Schoeberl, 1989; Chun & Kim, 2008; Kim & Chun, 2009; Snively & Pasko, 2003). Besides those numerical modeling studies to understand the generation mechanisms, various observational studies have been carried out to prove the existence of secondary GWs and to analyze their spectral characteristics in the real atmosphere. Wrasse et al. (2006) and Kim et al. (2010) demonstrated that about 70% of the observed GWs originated from the lower mesosphere by using ray-tracing analysis with all-sky camera (ASC) observations at Brazil (23°S) and South Korea (36°N), respectively. As for the secondary GWs in Antarctica, Matsuda et al. (2017) reported the possibility of the secondary wave generation over Davis station (68.57°S, 77.97°E) from ASC observations. Chu et al. (2018) showed, using lidar observations at McMurdo station (77.83°S, 166.67°E), the existence of secondary GWs by comparing different characteristics of the observed GWs in the mesosphere and lower thermosphere (MLT) and the stratosphere, which are reported previously in Chen et al. (2016) and Zhao et al. (2017), respectively.

In this study, we investigate GW activities in the upper mesosphere observed from the meteor radar at KSS for 14 years (2007–2020) and the possible sources of the observed GWs. The GW activities are estimated by extracting small-scale wind variances from the observed meteor echoes, and their long-term variabilities are investigated. The possibility for orography to be a potential source of observed GWs is examined based on the vertical profile of wind at KSS and upstream surface wind impinging on local topography near KSS. The potential nonorographic sources of observed GWs in the upper mesosphere at KSS are examined by calculating the correlation coefficients between the observed wind variance at KSS at $z = 96.8$ km and two diagnostics for (i) the jet-induced GWs (RNBE at 5 hPa) and (ii) convective GWs (convective GWs' momentum flux [CGWMFs] at 1 hPa) poleward of 30°S. In addition, the possibility of generation of the secondary GWs is examined by ray-tracing analysis with the ASC observations over KSS.

The structure of this paper is as follows: Section 2 describes the meteor radar observations and methodology used to extract GWs from meteor echoes. The airglow observations and backward ray-tracing analysis with the observed airglow images are also described. In Section 3, we investigate the characteristics of upper mesospheric GWs observed from the meteor radar. Differences in the magnitudes and seasonal variations in GW variances between the current study and several previous studies using meteor radar observations from Antarctic stations are discussed. The long-term (~14 years) variation of GW activities over KSS is also examined. Then, three major potential sources in the lower atmosphere (i.e., orography, polar night jet, and convection) are investigated by examining their relationships with observed GWs in the upper mesosphere. The generation of secondary GWs is discussed as another potential source of the observed GWs. Summary and discussion are given in Section 4.

2. Data and Methodology

2.1. VHF Meteor Radar Data

As meteors enter the Earth's atmosphere, plasma trails are formed by the friction of meteors with air. The decay times, radial velocities, and spatial information (e.g., azimuth angle, zenith angle, and radial distance) of meteor echoes are obtained by the five receiving antennas of a meteor radar system when the meteor echo signals backscattered from the meteor trail are perpendicularly aligned with the line-of-sight of the radar. The meteor radar at KSS can detect ~15,000–28,000 meteor echoes each day regardless of weather conditions (Lee et al., 2013).

Figure 1 shows the horizontal distribution of meteor echoes observed by the meteor radar at KSS during 00–01 UTC on January 15, 2014. KSS, marked by a red star (Figure 1a), is located on King George Island (KGI) north of the Antarctic Peninsula. Altitudes of observed echoes range from 80 to 100 km, as is indicated

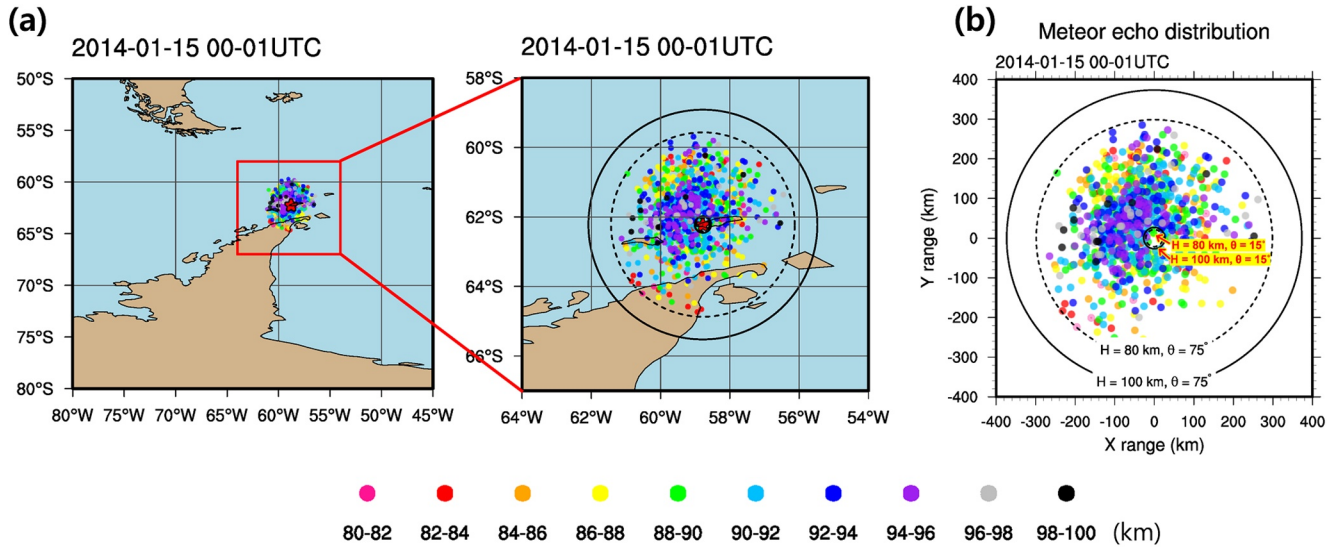


Figure 1. (a) Maps of the Antarctic Peninsula region. The colored dots indicate the positions of the meteor echoes detected by the meteor radar at King Sejong Station (KSS) from 00 to 01 UTC on January 15, 2014. The red star denotes the location of KSS (62.22°S, 58.78°W). (b) Horizontal distribution of all meteor echoes during the one hour projected onto the x - y plane. The color of each dot represents the altitude range where each echo is observed, and the altitude range corresponding to each color is shown in the legend. The black solid (dashed) inner and outer circles represent zenith angles of 15° and 75° for a height of 100 km (80 km), respectively.

by the colors of the dots used to represent echo positions in Figure 1. Most of echo positions are enclosed by the solid and dashed circles for the zenith angles of 15° and 75° at altitudes of 80 and 100 km, and this result indicate that most of meteor echoes are observed within the zenith angles of 15° and 75° (a radius of 300 km) in the altitude range between 80 and 100 km. Large-scale horizontal winds and GW variances are estimated using meteor echoes within the two zenith angles.

In mid-2007, early 2008, late 2009, early 2010, and mid-2018, the observations were suspended due to repair work, but the meteor radar observations at KSS have generally been uninterrupted since 2011. In the present study, monthly averages are computed only for months when more than 15 days of observations were conducted. In addition, data in March 2007, August 2009, and January 2016 were not used in the analysis because they included errors due to software or equipment problems (Lee et al., 2013).

The hourly zonal and meridional components of horizontal winds are estimated from radial velocities in a time-height bin of 2-h (incremented by 1-h intervals) and 3 or 5 km using the method in Hocking and Thayaparan (1997). Based on Mitchell and Beldon (2009), the following six height gates are used for binning observed echoes: (78–83), (83–86), (86–89), (89–92), (92–95), and (95–100) km. Representative heights for each height gate are 81.1, 84.6, 87.5, 90.5, 93.3, and 96.8 km, respectively, as in Mitchell & Beldon (2009) and Mitchell et al., (2002). At each time-height bin, the bin-averaged horizontal wind (U , V) is computed by solving the linear equation written as

$$U \sum_{i=1}^N l_i^2 + V \sum_{i=1}^N l_i m_i = \sum_{i=1}^N V_{r(ops),i} l_i, \quad (1)$$

$$U \sum_{i=1}^N l_i m_i + V \sum_{i=1}^N m_i^2 = \sum_{i=1}^N V_{r(ops),i} m_i. \quad (2)$$

Here, l_i and m_i are direction cosines. N represents the number of detected meteor echoes within each time-height bin, and $V_{r(ops),i}$ represents the observed radial velocity from the i -th meteor echo. In this study, the vertical wind velocity is ignored as magnitude of the vertical wind is much smaller than that of the horizontal winds (Mitchell & Beldon, 2009).

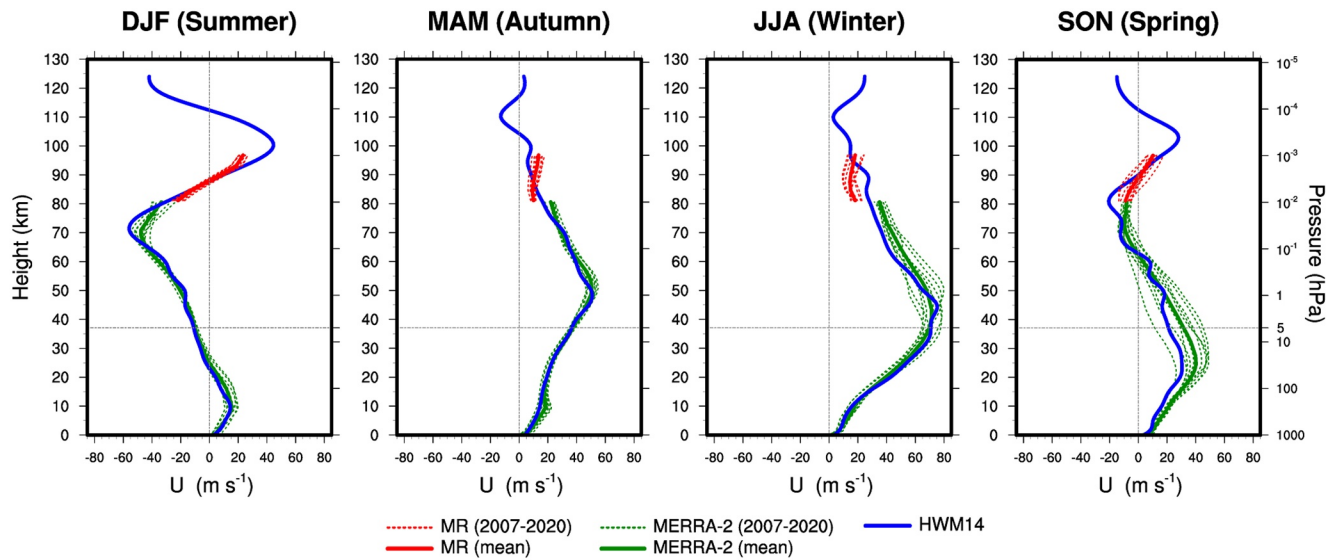


Figure 2. Seasonal climatologies of the vertical profiles of the zonal winds (blue solid lines) at King Sejong Station (KSS) obtained from the empirical Horizontal Wind Model (HWM14). Seasonally averaged zonal winds observed by the meteor radar (MR) at KSS during 2007–2020 (red dotted lines), with the 14-year mean value (red solid lines), are overlaid on each profile. Zonal winds of the Modern-Era Retrospective Analysis for Research and Applications, Version 2 (MERRA-2) on model levels at a grid point closest to KSS (green solid and dotted lines) are additionally used for comparison of the zonal winds below 0.01 hPa (~ 80.6 km). The three consecutive months used for the monthly average calculations are used to calculate the seasonal averages.

This linear equation set is obtained by minimizing the squared difference, in a least squares sense with at least six echoes, between the observed radial velocity and the radial component of the winds to be estimated. The squared difference is defined by

$$\varepsilon^2 = \sum_{i=1}^N \left(V_{r(mod),i} - V_{r(obs),i} \right)^2. \quad (3)$$

Figure 2 shows seasonal climatologies of the vertical profiles of zonal winds observed by the meteor radar at KSS, zonal winds obtained from the empirical Horizontal Wind Model (HWM14; Drob et al., 2015) at the location of KSS, and zonal winds from the Modern-Era Retrospective Analysis for Research and Application, Version 2 (MERRA-2; Gelaro et al., 2017) at a grid point closest to KSS. The seasonal average for each year is calculated only when there are sufficient observational data during three months for each season. As a result, 10, 10, 9, and 11 profiles of the seasonal-mean zonal winds are obtained in summer, autumn, winter, and spring for the 14 years, respectively. In summer and spring, the winds from the HWM14 and meteor radar are quite similar to each other in terms of both magnitude and wind shear, while in winter and autumn, discrepancies between the two are large. In the observational database employed by the HWM14 (see Drob et al., 2008, 2015), MF Radar data at the Davis station are the only Antarctic mesosphere observations (Douglas Drob, personal communication, 2021). Therefore, winds in the upper mesosphere over KSS may not be properly represented by planetary-scale spherical harmonics (used in the HWM) that are only constrained by observations at Davis station in the East Antarctica far from KSS. Besides, the HWM14 wind profile is similar to the zonal-mean profile obtained from the Committee on Space Research (COSPAR) International Reference Atmosphere (CIRA-86) data (Fleming et al., 1990). As a result, the large discrepancies between meteor radar and HWM14 in winter and autumn compared with summer and spring may be related to significant planetary-scale variations of the horizontal winds in the Southern upper mesosphere in winter and autumn that are not yet properly represented by the HWM14. It is also found in winter and autumn that the zonal winds obtained from the MERRA-2 reanalysis around $z = 80$ km are quite different from meteor radar observations. This difference may also be attributed to underestimated planetary-scale variations of the large-scale horizontal winds in the reanalysis. The reliability of the MERRA-2 reanalysis can be reduced in the upper mesosphere near the top boundary of the model (NASA Goddard Earth Observing System, Version 6; GEOS-6) used in the production of the reanalysis because of uncertainties of GW

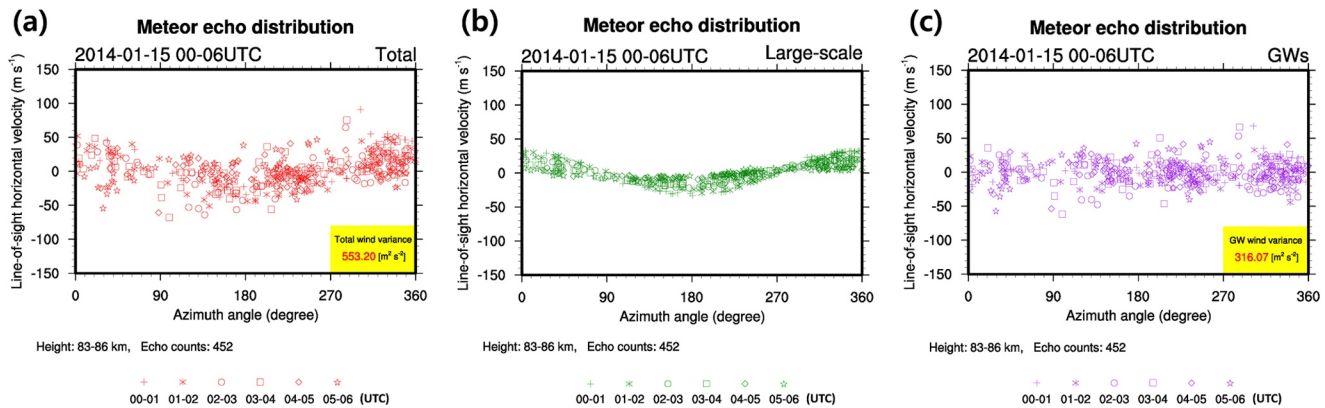


Figure 3. Azimuthal distributions of (a) the total line-of-sight horizontal winds observed at an altitude range of 83–86 km during 00–06 UTC on January 15, 2014 over King Sejong Station (KSS), (b) the line-of-sight components of the large-scale winds interpolated at each meteor echo positions, and (c) the difference (total minus large-scale winds) between panels (a) and (b). The differences shown in panel (c) are considered to be the small-scale gravity wave (GW) wind components. The different markers represent the different observation times with 1-h intervals. The variances of the observed and GW line-of-sight horizontal winds are shown in the bottom right of panels (a) and (c), respectively.

drag parameterization and artificial damping processes (Fujiwara et al., 2017), although the MLS data are assimilated into the GEOS-6 model (Gelaro et al., 2017).

2.2. Estimating GW Activities

In order to estimate small-scale GW activities in the upper mesosphere, the horizontal wind variance is calculated from the simple meteor-variance technique proposed by Mitchell and Beldon (2009). The GW wind variance represents the total level of wind perturbations by small-scale GWs within each time-space bin. The calculation process of the GW wind variance consists of three steps: (i) observation of radial velocities at each meteor echo position and converting to total line-of-sight horizontal velocities, (ii) estimation of large-scale horizontal winds (see Section 2.1) and their interpolation into each echo position, and (iii) calculation of the GW wind variance after removing the interpolated large-scale winds from the observed total winds. Figure 3 shows an example of the GW wind variance calculation for a specific time period (00–06 UTC on January 15, 2014) at $z = 83\text{--}86$ km. The horizontal GW wind variance is computed using the perturbations of line-of-sight horizontal winds (Figure 3c) after removing the line-of-sight components of the interpolated large-scale winds (Figure 3b) from the observed total line-of-sight horizontal winds (Figure 3a) at individual echo positions. The wind perturbations collected within 6-h intervals are used to calculate GW variances (i.e., 6-hourly variances) at each of six height gates from 81.1 to 96.8 km ([81.1–83], [83–86], [86–89], [89–92], [92–95], and [95–96.8] km). Here, the 6-h interval is chosen to increase the number of meteor echoes within each time-height bin for accurate wind variance calculations following Beldon (2008) and Mitchell and Beldon (2009). We examined the sensitivity of calculated GW wind variance according to the length of the time interval of collecting the wind perturbation, using the time intervals of 4 and 8 h, respectively. It is found (not shown) that the time interval does not significantly affect the estimated GW variance. Considering that the depths (1.8–3 km) of the six height gates are smaller than a scale height ($H \sim 5\text{--}7$ km), the effect of the GW amplitude growth ($e^{\Delta z/(2H)} < 1.2\text{--}1.4$, where $\Delta z = 1.8\text{--}3$ km) due to the exponential density decrease on the GW wind variance may be small. Given that the size of the time-height bins and the field of view of the meteor radar determine the scales of detected waves, GWs obtained from this methodology have periods less than 2 h, horizontal wavelengths up to 400 km, or vertical wavelengths less than 3–5 km. Therefore, IGWs with relatively long periods (3–10 h) and long horizontal wavelengths (a few thousands of km) observed by the lidar at McMurdo station (Chen et al., 2013, 2016) are hardly detected in this study.

To obtain reliable GW activities, following two checks are carried out in the horizontal wind variance calculation: (i) sufficiency of meteor echo counts and (ii) errors in the observed radial velocities. First, to avoid unreliable mean winds and wind variances due to insufficient echo counts (Hocking & Thayaparan, 1997; Mitchell & Beldon, 2009), wind variances are calculated only when at least 30 meteors were detected in the

time interval of 6 h. The diurnal cycle in the meteor echo counts does not affect seriously daily variations of the wind variances, as reported by Beldon and Mitchell (2010). As for seasonal variation of meteor counts, the monthly mean meteor echoes have little correlation with the monthly mean GW wind variances in most of height gates except for the lowest gate (not shown). In fact, the coefficient of determination (R^2 , where R is the correlation coefficient) between monthly mean meteor echo counts and GW wind variances is close to zero ($R^2 = 0.03$) for the entire observation period (Figure S1), implying that the effect of seasonal variation of meteor counts is negligible as well. Second, errors in the observed line-of-sight horizontal wind velocities for individual meteor echoes are considered. More than half of the meteor echoes have errors of less than 0.5 m s^{-1} , and 99% of them have errors of less than 3.5 m s^{-1} (Figure S2a). Consequently, errors in the horizontal GW wind variances, defined by the average of the squared individual errors (see Beldon, 2008 for details), are less than $1.5 \text{ m}^2 \text{ s}^{-2}$ (Figure S2b), which are negligibly small compared to the mean value of the GW wind variances (less than 0.25%). For temporal averaging, a geometric mean is used, given that the horizontal GW wind variances follow a log-normal distribution as discussed in Baumgaertner and McDonard (2007) and Mitchell and Beldon (2009).

2.3. Airglow Images Observed by an ASC and Backward Ray-Tracing Analysis

GW activities estimated by the wind variances can represent the total level of perturbations of winds due to multiple GWs within a given collecting volume of the meteor radar, but individual GWs cannot be resolved in the collecting volume. Therefore, it is difficult to distinguish the effects of GWs with different wave spectra on the GW wind variances observed from the meteor radar. As discussed in several previous studies, secondary GWs can be generated by the breaking of primary GWs and have different wave spectra from the primary GWs. In order to examine the secondary GWs observed in the MLT over KSS and their generation in the lower atmosphere, a backward ray-tracing analysis with airglow observations from the ASC at KSS is conducted.

The wave parameters estimated from ASC airglow observations are horizontal wavelengths, periods, and phase speeds. It is noteworthy that vertical wavelengths can also be estimated by using the airglow imager and lidar together (Lu, Chu, et al., 2015). The ASC observes GWs at $z = 87 \text{ km}$ through the OH Meinel band and at $z = 96 \text{ km}$ through the OI 557.7 nm airglow, respectively. The GWs observed through the ASC generally have horizontal wavelengths of 10–50 km and period of less than 1 h that can be included in the spectral ranges of the GWs observed using the meteor radar (Mitchell & Beldon, 2009). More details about the ASC and the GWs observed using the ASC at KSS can be found in Kam et al. (2017). In this study, we use 8-year (March 2008–October 2015) GW parameters estimated from the ASC observations at KSS as input parameters for the reverse ray tracing. It is noted that the ASC observations at KSS have been carried out from March to October to avoid the period of the midnight sun. For the ray tracing, the GW Regional Or Global Ray Tracer (GROGRAT) model (Marks & Eckermann, 1995) is employed, and for the background winds and temperature, the ground-to-space (G2S) data (Song et al., 2018) made by fitting spline curves to reanalyzes (ERA-Interim and MERRA) in the lower atmosphere and empirical model results (HWM14 and NRLMSISE-00) above the stratopause. Rays in the GROGRAT are terminated when (i) GWs become evanescent ($m^2 < 0$; m is the vertical wavenumber), (ii) the intrinsic frequencies are close to zero or become negative, (iii) the WKB approximation is violated, and (iv) rays reach domain boundaries.

3. Results

3.1. GW Activities

Figure 4 shows the time series of the daily averaged GW wind variances for 2007–2020 along with the 14-year climatology of monthly averaged GW wind variances and the time series of the monthly averaged wind variances during the entire observation period in the last two panels. As discussed in Section 2.2, the GW wind variances represent the activities of GWs with periods ($< 2 \text{ h}$), horizontal wavelength ($< \sim 400 \text{ km}$) or vertical wavelength ($< 3\text{--}5 \text{ km}$). GW activity in the upper mesosphere shows semiannual variations especially below $z = 90 \text{ km}$, with a primary peak in winter, secondary peak in summer, and two minima during the equinoxes. The seasonal variations in GW activities at KSS are quite similar to those at other Antarctic stations. Vincent (1994) observed the semiannual variations in GW activities using MF radar, with maxima

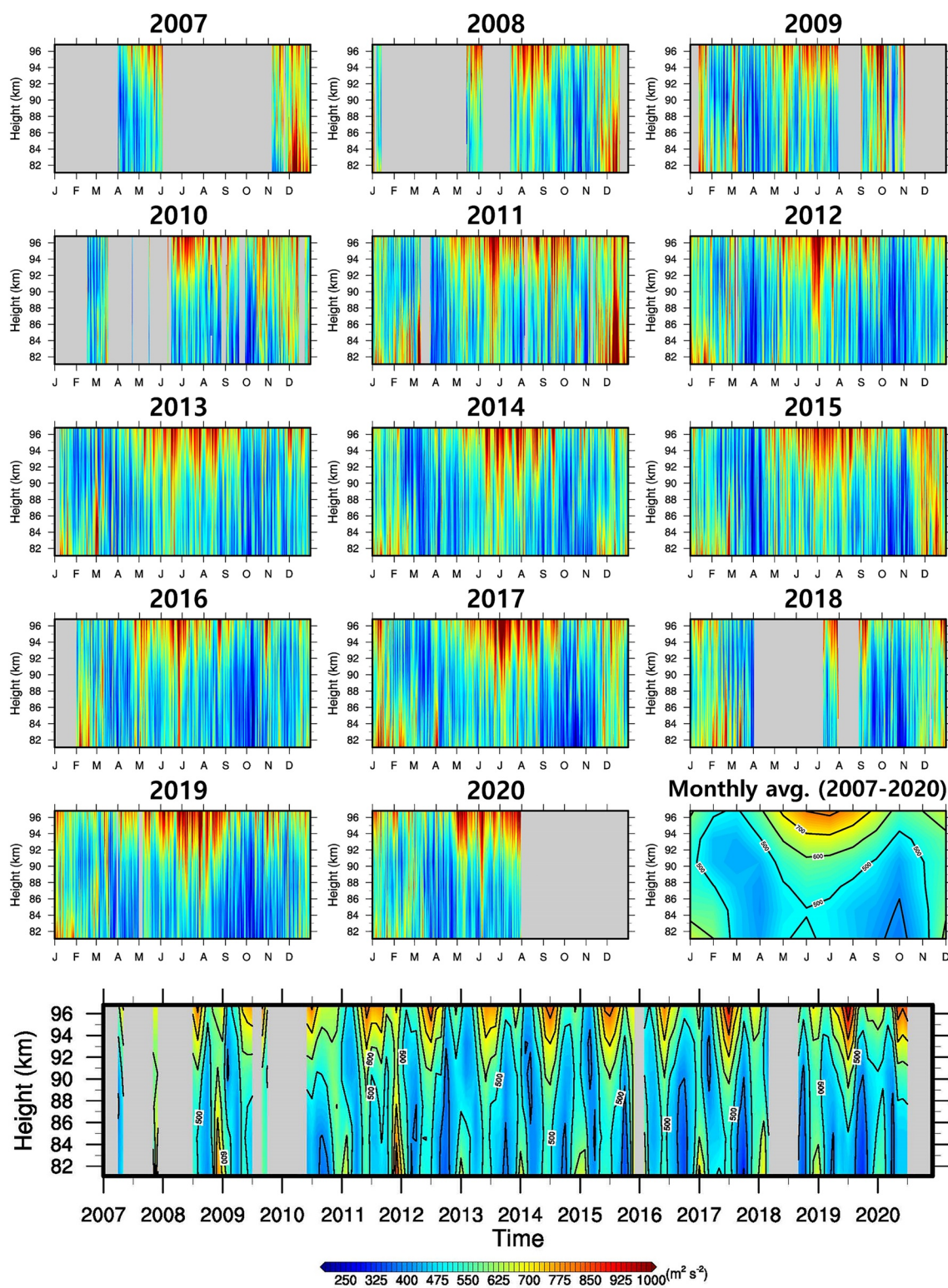


Figure 4. Time-height cross sections of the daily averaged horizontal gravity wave (GW) wind variances observed from the meteor radar at King Sejong Station (KSS) during 2007–2020. The 14-year mean monthly averaged horizontal GW wind variances and time series of the monthly averaged wind variances during the entire observation period are shown in the last two panels.

occurring during the solstices at Mawson station (67.60°S, 62.87°E). Similar results are also shown at the Davis and Syowa stations (Dowdy et al., 2007) and Rothera station (Mitchell & Beldon, 2009). The semiannual variations in GW activities have been explained by the saturation-limit amplitude of GWs (Connor & Avery, 1996; Dowdy et al., 2007; Isler & Fritts, 1996; Lindzen, 1981; Mitchell & Beldon, 2009). According to the linear saturation theory of internal GWs by Lindzen (1981), the amplitude of GWs cannot be increased above the wave-breaking level because turbulence induced by wave breaking exactly cancels the amplification via the decrease in density above the wave-breaking level. That is, the amplitude of u' is limited by $|u'| \leq |\hat{c}| = |c - \bar{u}|$, where \hat{c} represents the intrinsic phase speed, c represents the ground-relative phase speed, and \bar{u} represents the background wind. For stationary waves, the GW amplitude becomes the magnitude of the background wind when it is saturated. Because the background wind speed at high latitudes in the SH has semiannual variations, with the strongest in the solstices and the weakest in the equinoxes, GW activities can also have semiannual variations in the upper mesosphere. In the stratosphere and lower mesosphere at KSS, the amplitudes of zonal wind from the MERRA-2 data have a clear annual periodicity, with a strong westerly (easterly) jet in winter (summer) (see Figure 2). These results support the linear saturation theory, which explains the semiannual variations in GW variances below $z = 90$ and is likely applicable to non-stationary GWs with relatively small c than \bar{u} as well. Above $z = 90$ km, however, the annual variations in GW activities are pronounced in addition to the semiannual variations. These annual variations are likely due to the decreased GW activities near the summer mesopause (~ 90 km) and the strong GW activities in winter. The decreased wind variances at the mesopause during summer are also observed at Rothera station (Beldon & Mitchell, 2010). In addition, the annual variation may also be attributed to the critical-level filtering by the mean winds, which will be discussed in following section.

During the same observation period (2011–2014), GW wind variances at KSS are about 1.1–1.3 times smaller than those at Rothera station (Figure S3). Given that Rothera station is located more than 700 km from KSS toward Antarctic continent, different GW activities in the two stations can be attributed to different GW sources. In particular, the relative position of the edge of the polar night jet over SH polar regions may have affected the different GW activities at the two stations. Further research on the comparison of GW wind variances between the two stations may be needed in the future to understand the differences in GW activities with respect to geographical locations and GW sources, once sufficient meteor radar data observed at the two stations during the same period are available.

In order to investigate the long-term variability of the GW activities over KSS, the monthly averaged horizontal wind variance at each height gate during 2007–2020 are shown in Figure 5a, after deseasonalizing by subtracting the 14-year averaged values of each month and linear detrending. The red lines indicate the 3-month running averaged values. The green curves represent the second-order least squares polynomial fitted values. Above $z = 90$ km, GW activities tend to decrease until 2014–2015 and increase since 2015, while there are no clear long-term trends on GW activities below $z = 90$ km. The long-term variation of the GW activities above $z = 90$ km (especially at $z = 96.8$ km) seems to relate to the 11-year solar cycle. A statistically significant peak at approximately 11-year is shown in the Lomb-Scargle periodogram (Lomb, 1976; Scargle, 1982) of the horizontal wind variance at $z = 96.8$ km (Figure S4). There are no other statistically significant interannual and long-term variation of the GW activities in the MLT over KSS.

Monthly averaged $F_{10.7}$ index, a proxy of solar activity (Tapping, 2013), is used to compare with the observed GW activity in the upper mesosphere at KSS (Figure 5b). The $F_{10.7}$ have maximum value during 2014–2015 while minimum values exist in 2008–2009 and 2019–2020, showing negative correlation with the long-term variations of the GW activities above $z = 90$ km. The negative correlation, however, is not found below $z = 90$ km. Ern et al. (2011) showed that GWMFs in the stratosphere and mesosphere observed by satellite instruments have time variations negatively correlated with 11-year solar cycle. Park et al. (2014) also found, using the Challenging Minisatellite Payload (CHAMP) satellite, the negative correlation between the solar activity and GW activity in the thermosphere. However, it is noteworthy that the correlation between the GW activities in the MLT and solar activities is somewhat controversial and likely depends on observation location. For example, Gavrilov et al. (1999) and Jacobi et al. (2006) showed that positive correlations appeared between the solar activity and GW activity over Japan and Germany, respectively. Therefore, as pointed out in Ern et al. (2011), a longer period of data collection is required to clearly show the relationship between the solar cycles and the GW activities in the MLT over KSS.

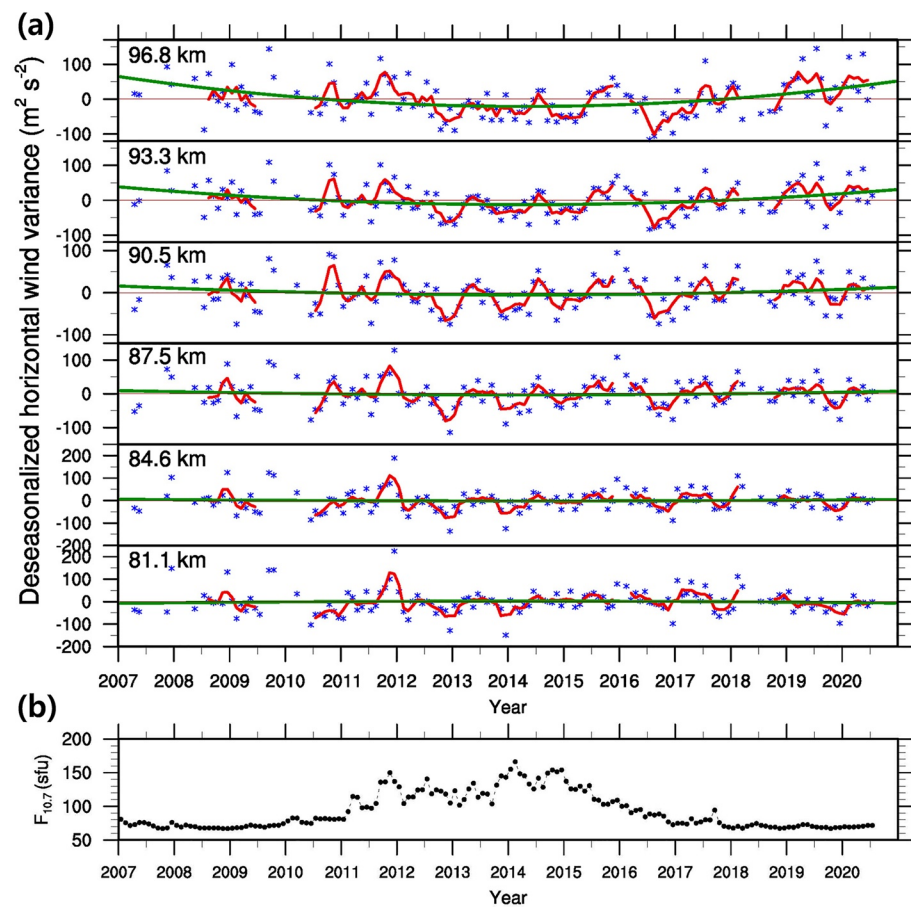


Figure 5. (a) Time series of monthly averaged values of deseasonalized and linearly detrended horizontal gravity wave (GW) wind variances (blue asterisks) calculated in six height gates with representative heights of 81.1, 84.6, 87.5, 90.5, 93.3, and 96.8 km, respectively. The red lines indicate the 3-month running-mean GW wind variances. The green lines indicate the second-order polynomials least squares fit to GW wind variances. Note the ranges of the ordinate are different depending on the representative heights. (b) Time series of monthly averaged the 10.7 cm solar radio flux ($F_{10.7}$) expressed in solar flux units (sfu; $1 \text{ sfu} = 10^{-22} \text{ W m}^{-2} \text{ Hz}^{-1}$).

It is noteworthy that the deseasonalized and linearly detrended GW wind variances are maximum in most altitudes in December 2011 (Figure 5a). We found that (not shown), there were no significant changes in the wave sources and/or propagating conditions in December 2011. One possible mechanism for the growth of GW activities in the MLT region is the GW modulation by the diurnal tides (DTs). Using Doppler radar observations over Australia, Fritts and Vincent (1987) demonstrated that the GWs in the MLT region can be modulated by the DT components. Similar results were obtained from the meteor radar observations at Rothera station by Beldon and Mitchell (2010) as well. The amplitude of the DT at KSS calculated using the present data is quite strong in December 2011, but exclusively below $z = 90 \text{ km}$ (Figure S5). The possibility of GW enhancement by the GW-DT interaction in December 2011 is beyond the scope of this paper, which remains for the future research topic.

3.2. Potential Sources of GWs

3.2.1. Orography

As mentioned earlier, the strong wind variances in winter shown in Figure 4 can be related to stationary orographic GWs. We examine the possibility of the generation of orographic GWs and their propagation into the MLT region in each season. Figure 6a shows the map of KGI and seasonally averaged wind vectors at 925 hPa ($\sim 0.55 \text{ km}$) for 8 years (2012–2019). The wind vectors are obtained from the MERRA-2 data at

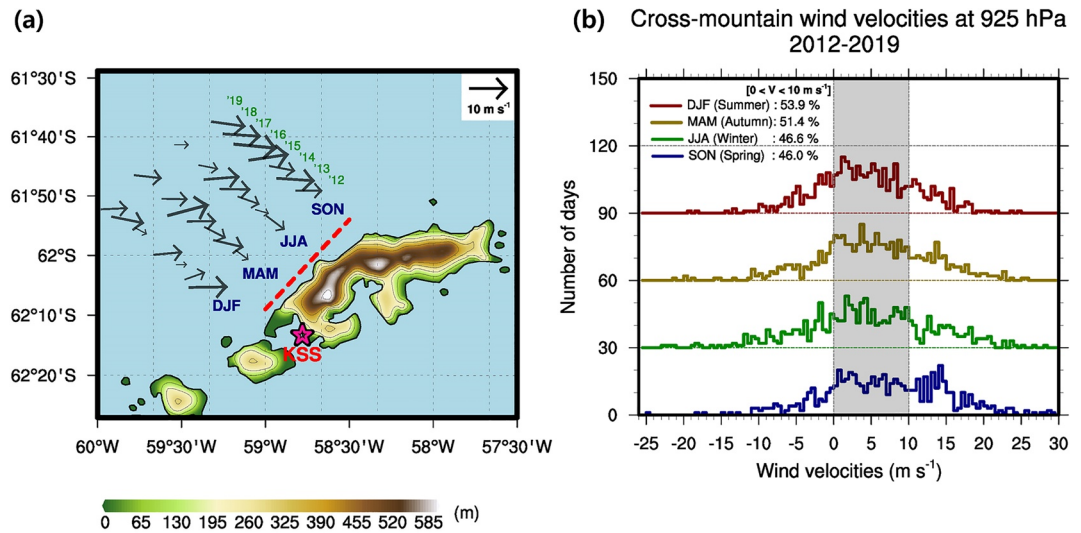


Figure 6. (a) Seasonally averaged horizontal wind vectors at 925 hPa (~ 0.55 km) over King George Island (KGI) during 2012–2019. For horizontal wind data, the MERRA-2 reanalysis data at the grid point closest to the northwest side of KGI (62.0°S , 58.75°W) are used. The red dashed line indicates the direction along the mountain range near King Sejong Station (KSS). The pink star denotes the location of KSS (62.22°S , 58.78°W). (b) Seasonal histograms of daily averaged cross-mountain wind velocities at 925 hPa over KGI during 2012–2019. The y-axes are offset by 30 for clarity. The percentages of days with weak orographic forcing conditions ($0\text{--}10\text{ m s}^{-1}$) during each season are shown in the upper left corner of panel.

the grid point (62.0°S , 58.75°W) northwest of the KGI and closest to KSS. KSS is located on KGI with steep mountains and orographic GWs can be generated by cross-mountain flows near KSS (i.e., southeastward flows). The southeastward winds mainly occur in winter (JJA) and autumn (MAM). In addition to the wind direction, the strength of the cross-mountain wind (i.e., orographic forcing) is another factor in determining the generation of orographic GWs that can reach the MLT region. Indeed, orographic GWs generated by relatively weak orographic forcing propagate readily into the MLT region, while large-amplitude GWs generated by strong orographic forcing can be broken in the upper stratosphere and lower mesosphere generating secondary GWs (Bossert et al., 2017; Fritts et al., 2019; Taylor et al., 2019). Figure 6b shows the seasonal histograms of daily averaged cross-mountain wind velocities at 925 hPa during 2012–2019. There are no distinct seasonal differences in the percentages of days satisfying the weak orographic forcing condition ($0\text{--}10\text{ m s}^{-1}$). Therefore, orographic GWs can be generated and propagate into the MLT region in any season under the weak orographic forcing condition without wave breaking.

Table 1
Seasonally Averaged Percentages of Mountain Wave Propagation Days When the Horizontal Wind Vector Rotates Less Than 90° from the Direction of the Mountain Range Northwest of the KGI With Heights Between 925 hPa and 0.01 hPa.

	DJF	MAM	JJA	SON	(%)
2012	8.8	48.9	58.7	34.1	
2013	25.6	66.3	64.1	34.1	
2014	41.1	52.2	64.1	27.5	
2015	14.4	71.7	81.5	41.8	
2016	-	63.0	80.4	42.9	
2017	38.9	72.8	75.0	29.7	
2018	12.2	-	-	29.7	
2019	20.0	65.2	60.9	-	
Average	23.0	62.9	69.2	34.3	

However, a critical-level filtering effect should also be considered in order to assess the possibility of propagation of orographic GWs into the MLT region. Following Yamashita et al. (2009), we calculate the percentages of days when the rotation of the horizontal wind vector is less than 90° at an altitude range of 925–0.01 hPa, under the assumption that GWs are filtered if the rotation exceeds 90° , and the results are shown in Table 1. The 8-year averaged percentage is the highest in winter (69.2%), and the next highest (62.9%) occurs in autumn. The percentages in summer and spring are 23.0% and 34.3%, respectively. These results are consistent with steadfast westerlies throughout the troposphere and middle atmosphere in autumn and winter (see Figure 2). Hence, orography can be considered to be a highly potential source of observed waves in the upper mesosphere over KSS during autumn and winter. Some recent works during the Deep Propagating GW Experiment (DEEPWAVE) campaign (Fritts et al., 2016) also showed that orographic GWs can easily propagate into the winter mesosphere.

3.2.2. Polar Night Jet

Besides stationary GWs due to weak orographic forcing, the jet stream in the lower atmosphere can be a source of non-stationary GWs observed in the upper mesosphere. Yoshiki et al. (2004) demonstrated that GW activities can be enhanced in the polar lower stratosphere in autumn or spring when the Antarctic vortex is strengthened (autumn) or weakened (spring). In the present study, we use the RNBE as a diagnostic for the generation of GWs induced by jet stream as in previous studies (e.g., Ki & Chun, 2011; Song et al., 2017; Yoo et al., 2020; Zhang, 2004). The RNBE represents the imbalance of the large-scale flow associated with the jet stream. The RNBE in the spherical coordinate system (Chun et al., 2019) can be written as

$$RNBE = 2J(u, v) + f\zeta - \nabla^2\Phi - \beta u - D^2 - \frac{\partial \vec{V}}{\partial p} \circ \vec{\nabla} \omega + X, \quad (4)$$

$$D = \vec{\nabla} \circ \vec{V} = \frac{1}{a \cos \phi} \frac{\partial u}{\partial \lambda} + \frac{1}{a \cos \phi} \frac{\partial}{\partial \phi} (v \cos \phi), \quad (5)$$

$$X = -\frac{1}{a^2 \cos \phi} \frac{\partial}{\partial \phi} \left[(u^2 + v^2) \sin \phi \right]. \quad (6)$$

Here, u and v denote the zonal and meridional winds, respectively; $J(u, v)$ is the Jacobian, Φ is the geopotential, f ($2\Omega \sin \phi$, where Ω represents the angular speed of rotation of the Earth) is the Coriolis parameter, β ($= 2\Omega \cos \phi / a$) is the latitudinal derivative of f , ζ is the vertical component of relative vorticity, ω represents the pressure (p) velocity ($\equiv Dp / Dt$); D is the divergence; λ and ϕ denote the longitude, and latitude, respectively; a is the mean radius of the Earth. The RNBE is calculated using the 6-hourly European Centre for Medium-Range Weather Forecasts (ECMWF) Reanalysis (ERA) Interim data set (Dee et al., 2011). To exclude the resolved IGW components from the ERA-Interim data set, a low-pass filtering in the zonal direction is applied to the variables in Equations 4–6, with zonal wavenumbers less than 23 (Sato et al., 2009).

Figure 7a shows the polar stereographic projection maps of the seasonally averaged $|RNBE|$ and horizontal wind vectors at 5 hPa (~ 37 km) averaged over 8 years (2012–2019). Here, 5 hPa is chosen to represent the altitude of the polar night jet in the upper stratosphere. In winter (JJA), the $|RNBE|$ is large along the axis of the strong polar vortex centered around Antarctica, and it is particularly large east of the southern tip of the South America and in the Eastern Hemisphere. The $|RNBE|$ is larger in spring (SON) than in autumn (MAM), although the stratospheric jet is slightly stronger in autumn than in spring (see Figure 2). The intensity of the stratospheric jet and the $|RNBE|$ are the smallest in summer (DJF).

Figure 7b shows the correlation coefficients between the daily mean GW horizontal wind variance at $z = 96.8$ km obtained from the meteor radar observations at KSS and the daily mean $|RNBE|$ at 5 hPa for regions south of 30°S . Correlation coefficients are averaged over 8 years (2012–2019) for each season. The thick and thin black solid lines indicate areal boundaries of statistical significance at the 90% and 80% confidence level for the Student's t -test (Wilks, 2011), respectively. In summer (DJF), there is no significant correlation in most areas because of the weak polar night jet. In spring (SON) and autumn (MAM), there are significant positive correlations near the stratospheric jet. Interestingly, the correlations in winter are much smaller than those in autumn or spring, even though the largest $|RNBE|$ appears along the winter stratospheric jet (Figure 7a).

To understand the discrepancy between the $|RNBE|$ and the magnitude of the correlation coefficients shown in Figure 7b, we examine the possible ranges of the phase speeds of GWs associated with jet stream and their propagation and the dissipation processes in the stratosphere and mesosphere. It might be useful if there were available reports of modeling results about the phase speeds of GWs induced by the stratospheric jet stream, but, to the best of author's knowledge, there have been no systematic numerical modeling studies on the phase speed spectra of GWs generated by the stratospheric jet stream, although the generation of IGWs around the stratospheric jet stream has been revealed by some numerical simulations (e.g., Fairlie et al., 1990; Sato et al., 1999). Meanwhile, there have been some observational studies on the phase speed spectra of GWs associated with the stratospheric jet stream. Yamanaka et al. (1989)

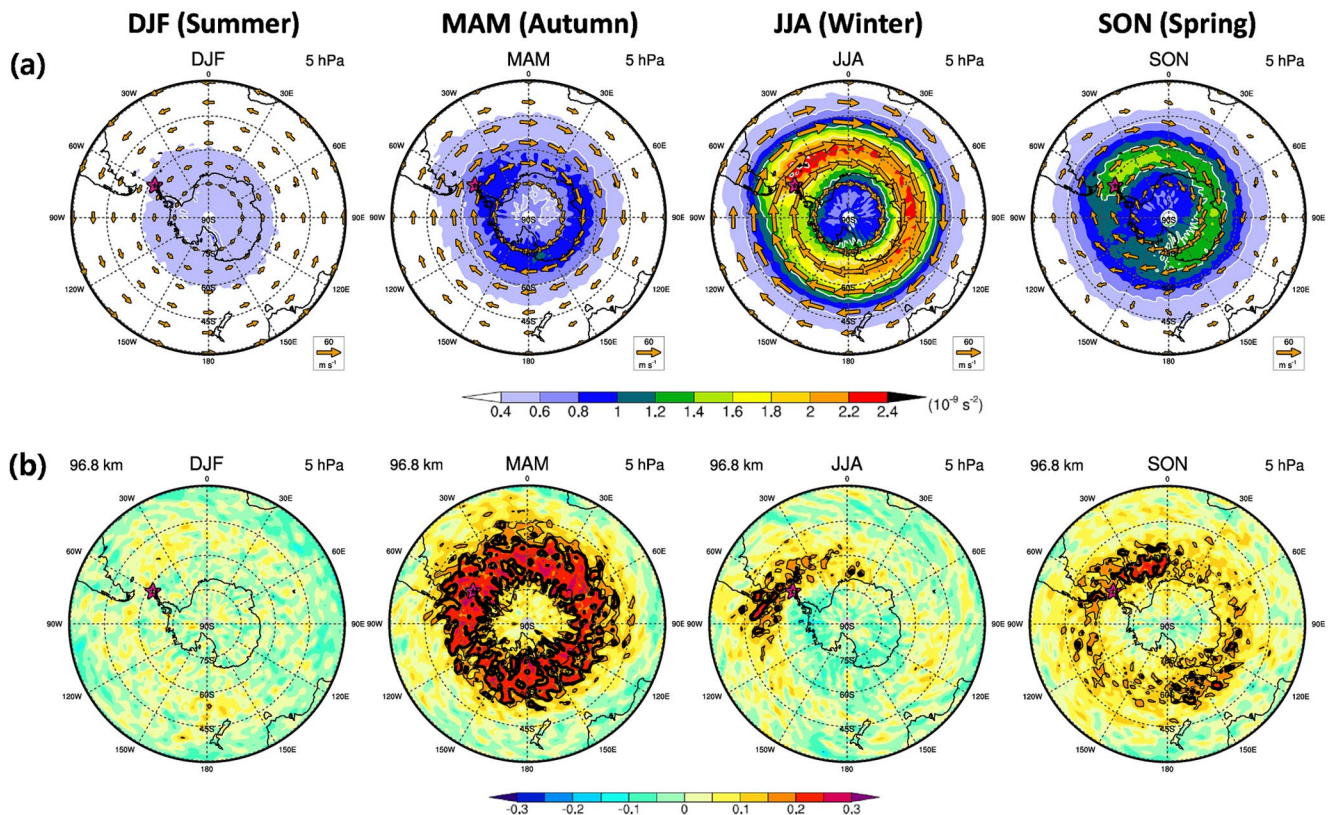


Figure 7. (a) Polar stereographic projection maps of seasonal mean $|RNBE|$ (shading) superimposed onto the horizontal wind vectors at 5 hPa in the SH. The RNBE is computed using the 6-hourly ERA-Interim reanalysis and then averaged over 2012–2019. The longitudinal (latitudinal) grid lines are drawn every 30° (15° starting from 30°S) with dotted lines. (b) Correlation coefficients between the daily mean $|RNBE|$ at 5 hPa and the daily mean horizontal GW wind variance at $z = 96.8$ km above King Sejong Station (KSS). The thick (thin) black solid lines denote statistical significance at the 90% (80%) confidence level. The pink star denotes the location of KSS (62.22°S, 58.78°W).

showed that the horizontal phase velocities of GWs above the jet stream observed from mesosphere-stratosphere-troposphere (MST) radars have a broad range (approximately -10 to 60 m s⁻¹) at the altitude range of 10–23 km. Murphy et al. (2014) observed the horizontal phase speed distribution of downward-propagating GWs in the height range of 15–31-km using a radiosonde launched at Davis station and showed that most GWs generated from the stratospheric jet have phase speeds with ranges of about ± 20 m s⁻¹ around the mean flow speed.

In case that the horizontal winds have strong negative vertical shear throughout the mesosphere, a great deal of jet-induced GWs propagating westward relative to the mean flow may be filtered out at their critical levels before they reach the upper mesosphere. As shown in Figure 2, the change in zonal wind throughout the mesosphere is largest in winter (about 70–10 m s⁻¹), and it is generally small in autumn (45–15 m s⁻¹) and spring (20 to -10 m s⁻¹). Therefore, only a small part of the westward (relative to the jet stream) propagating GWs induced by the substantially large RNBE east of KSS may survive the filtering and thus may possibly be observed at the mesopause height over KSS (see relatively large correlation between 30°–60°W in JJA shown in Figure 7b). In addition to the critical-level filtering, Doppler shifting via strong mean flow can explain the low winter-time correlation for the eastward propagating GWs relative to the mean flow. In winter, the polar night jet is the strongest, and the absolute value of intrinsic frequencies of jet-induced GWs propagating eastward relative to the mean flow become large when they propagate upward (i.e., upshear direction) in the mesosphere where the mean flow is smaller than the stratospheric polar night jet. GWs with those high intrinsic frequencies and long vertical wavelengths can reach the MLT region quickly (Baumgaertner & McDonald, 2007; Whiteway et al., 1997) without long horizontal propagation from the source region. Therefore, eastward (relative to the jet stream) propagating GWs generated by the stratospheric jet stream east of KSS with strong RNBE are unlikely to be observed at KSS at 96.8 km altitude. GWs

generated by weak RNBE on the far upstream (i.e., 120°–150°W) from KSS would not be observed either in the mesopause height over KSS because they can propagate quickly to the MLT region before they reach the horizontal location of KSS. Rather, GWs generated by relatively weak RNBE on the upstream close to KSS (i.e., 60°–100°W) that propagate eastward (relative to the jet stream) and upward can reach KSS in the upper mesosphere, which is evident from relatively strong correlation (Figure 7b). In spring and autumn when the wind shear is weak or moderate compared with winter, flow imbalance associated with the polar night jet in the upper stratosphere can be an important source of observed GWs in the upper mesosphere over KSS because jet-induced GW activities can increase in spring and autumn when the polar vortex starts breaking or recovering (Moffat-Griffin et al., 2011; Yoshiki et al., 2004).

3.2.3. Convection in Storm Tracks

Deep convection is another potential source of observed GWs in the upper mesosphere. There are only a few observational (e.g., Ern et al., 2011) and modeling (e.g., Choi & Chun, 2011) studies that have focused on convection as a source of GWs in the SH polar stratosphere and mesosphere. Here, we examine the possibility of convection as a potential source of observed GWs in the upper mesosphere over KSS using the CGWMF calculated through an offline CGWD parameterization described by Kang et al. (2017). To compute the CGWMF, the hourly wind, temperature, deep convective heating (DCH) rate, and cloud top and -bottom height information obtained from the National Centers for Environmental Prediction (NCEP) Climate Forecast System Reanalysis (CFSR) (Saha et al., 2010) are employed (see Kang et al., 2018, for details). The absolute value of the CGWMF is obtained by adding the magnitudes of the components of the CGWMF in the four Cardinal directions. The daily average absolute CGWMFs in four selected months (February 2009, April 2009, July 2010, and October 2010), when there were no missing meteor radar observations on a daily basis, are examined.

Figure 8a shows the polar stereographic projection map of the monthly mean of column-maxima of the DCH obtained from the CFSR data. The DCH shown in Figure 8a represents convective activities in the mid-to high latitudes (see the latitudinal grid lines drawn from 30°S). In autumn and winter, the large-scale aggregates of large DCH are found along the midlatitude storm-track regions surrounding Antarctica, but in spring and summer, weak DCH is scattered throughout the midlatitude regions. These spatial and seasonal structure of the DCH is also consistently found in a long-term data for 32 years (1979–2010) shown in Kang et al. (2017). In autumn and winter, the CGWMF at 1 hPa (~48 km) shown in Figure 8b is large in the high latitudes as well as in the storm-track regions where the DCH is large. The spatial difference between the DCH and CGWMF is because the CGWMF is determined not only by DCH but also by wave filtering and resonance. The wave filtering is affected by background wind structure, and the resonance is determined by the natural mode related to the vertical structure of convective heating (Kang et al., 2017; Song & Chun, 2005). The spatial structure of the CGWMF at 1 hPa in July 2010 is generally similar to the observed from SABER in July 2006 (see Figures 9b and 9d in Ern et al., 2011) in that large CGWMF is found above major southern storm-track regions (around the southern tip of the South America, south of the Africa, and around the Australia) as shown in Ern et al. (2011). However, the maximum magnitude of the CGWMF at 1 hPa in July 2010 is 2–3 times larger than that observed from SABER (Ern et al., 2011). This difference can be attributed to the fact that the range of horizontal wavelengths observed by the limb sounders like SABER or HIRDLS is longer than 100–200 km (Alexander, 2015; Ern et al., 2011; Trinh et al., 2016), while the predominant horizontal wavelengths of convective GWs considered in the CGWMF are smaller than 100–200 km. Because of this substantial spectral discrepancy, it is difficult to compare parameterization results with the limb sounder observations, even if the observational filters associated with the limb sounder observations are applied to parameterization results.

Figure 8c shows the correlation coefficients between the horizontal wind variance at $z = 96.8$ km and the absolute CGWMF at 1 hPa south of 30°S. In spring and summer, correlation coefficients are overall small and statistically insignificant. Meanwhile, in autumn and winter, significant positive correlations are evident in several regions where large CGWMFs exist. Although the high correlation regions are not very close to KSS, convective GWs in those regions at 1 hPa relatively close to KSS can possibly reach the upper mesosphere over KSS in that GWs in general can propagate toward the axis of the polar vortex that usually passes the location of KSS in autumn and winter (Kalisch et al., 2014; Sato et al., 2009; Song et al., 2020).

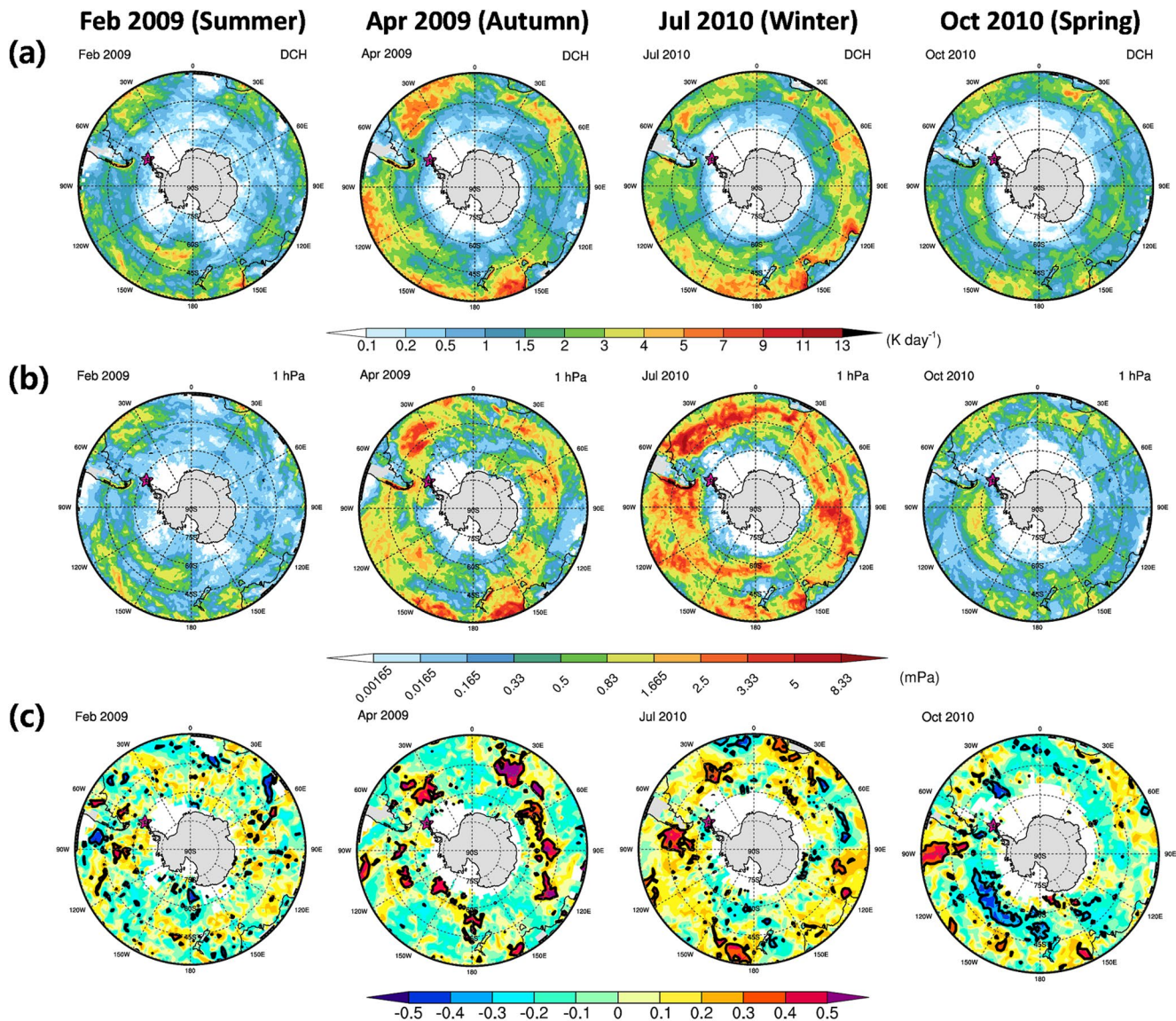


Figure 8. Polar stereographic projection maps of the monthly mean (a) column-maximum deep convective heating rate (DCH) and (b) absolute convective gravity wave momentum flux (CGWMF) at 1 hPa in February 2009, April 2009, July 2010, and October 2010. (c) Correlation coefficients between the daily mean absolute CGWMF at 1 hPa and the daily mean horizontal gravity wave (GW) wind variance at $z = 96.8$ km above King Sejong Station (KSS). The black solid lines denote statistical significance at the 90% confidence level.

In summary, convective clouds over SH mid-latitude storm track regions can be a possible source of GWs observed in the upper mesosphere over KSS in autumn and winter.

3.2.4. Secondary Gravity Waves Generated in the Mesosphere

Apart from relatively weak potential wave sources in the lower atmosphere described above (Sections 3.2.1–3.2.3), in-situ generation in the mesosphere can be an additional potential source of the observed mesospheric GWs. To check whether the sources of observed mesospheric GWs are located in the mesosphere or in the lower atmosphere, the reverse ray-tracing analysis is carried out using wave parameters observed using the ASC operating at KSS.

Figure 9 shows reverse trajectories of the rays for the GWs observed using the ASC at KSS during the 8 years. Among 131 traceable wave events (76 from OH and 55 from OI), 44, 12, and 75 events are terminated in the mesosphere ($z > 60$ km; Figure 9a), stratosphere ($z = 15$ –60 km; Figure 9b), and troposphere

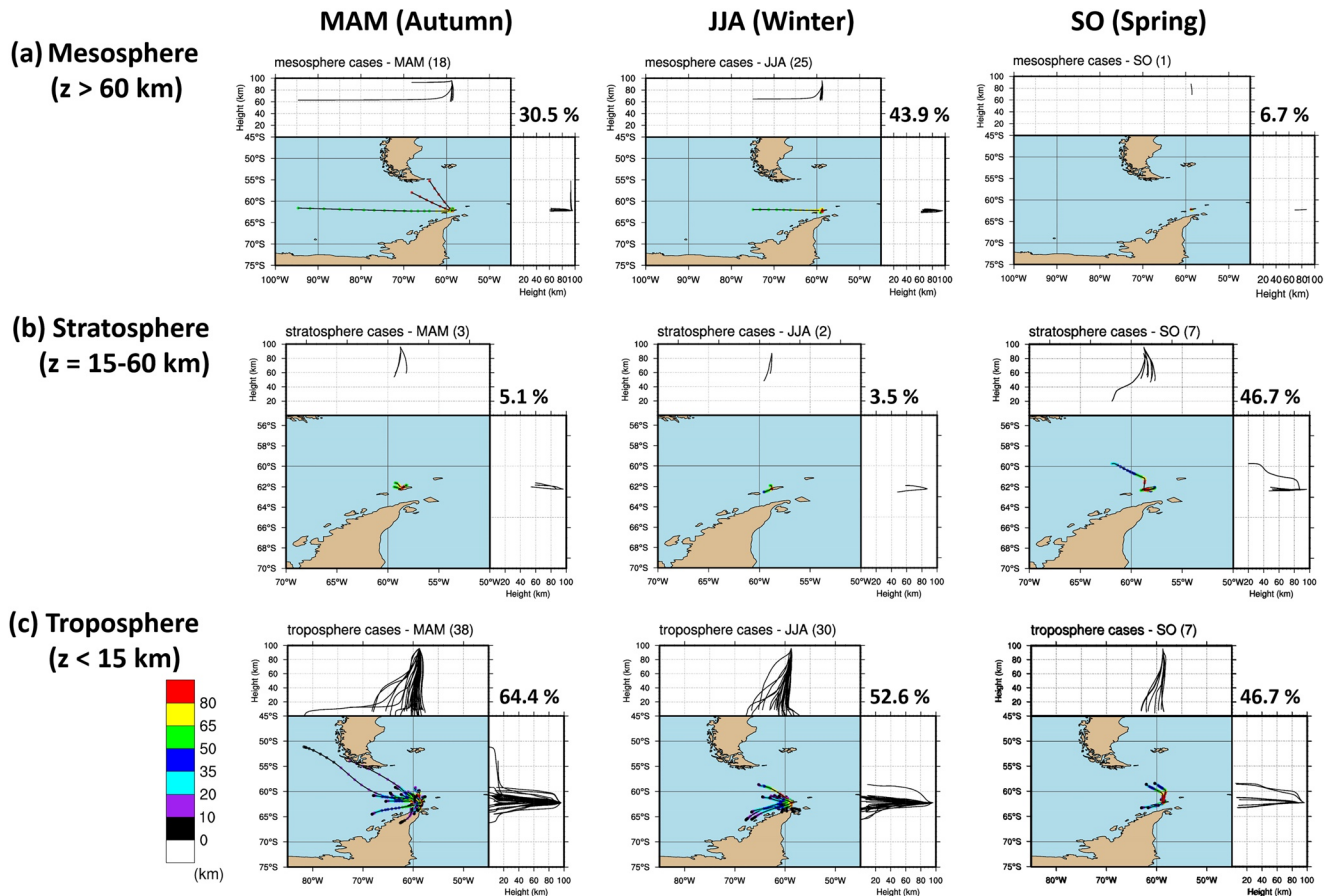


Figure 9. Reverse ray trajectories of the gravity waves (GWs) observed by an all-sky camera for OH and OI 557.7 nm airglows at KSS from March 2008 to October 2015. Wave source regions are classified into the three layers based on the ray termination heights: (a) mesosphere ($z > 60$ km), (b) stratosphere ($z = 15\text{--}60$ km), and (c) troposphere ($z < 15$ km). The percentages of wave events that terminated in each layer among the total wave events during (left) March–May, (middle) June–August, and (right) September–October are shown in the upper right corner of each panel.

($z < 15$ km; Figure 9c), respectively. Out of 59 (MAM), 57 (JJA), and 15 (SO) traceable wave events, 18 (30.5%), 25 (43.9%), and 1 (6.7%) events are terminated in the mesosphere, respectively. This implies that a large portion of the observed GWs in the mesosphere over KSS is the secondary GWs. In particular, orographic GWs reaching the mesosphere without experiencing critical-level filtering during winter (see Table 1) can contribute to the secondary GWs generation. Some recent studies investigated the secondary GWs associated with orography in wintertime from observations (e.g., Bossert et al., 2017) and numerical modelings (e.g., Becker & Vadas, 2018). Bossert et al. (2017) observed secondary GWs over New Zealand in winter during the DEEPWAVE campaign and demonstrated that the observed GWs are the secondary GWs associated with the mountain waves. Becker and Vadas (2018) showed the secondary GWs by breaking of orographic GWs during winter using the Kühlungsborn Mechanistic GCM (KMCM). The significant proportion of secondary GWs generated in winter mesosphere may also contribute to the low correlations between the GW activities in the mesosphere and $|\text{RNBE}|$ at 5 hPa during winter as shown in Figure 7b.

4. Summary and Discussion

GW activities in the upper mesosphere are investigated using meteor radar observations at KSS (62.22°S, 58.78°W) in the Antarctic Peninsula for 14 years (2007–2020). The observed horizontal winds and their seasonal variabilities are consistent with the well-established climatology at SH high latitudes. GW activities in the upper mesosphere are estimated by the wind variance, which is calculated using a simple meteor-variance technique. The wind variances are sensitive to GWs with relatively short periods (< 2 h), short

horizontal wavelength ($< \sim 400$ km) or short vertical wavelength ($< 3\text{--}5$ km). GW variances have semiannual variations (with a primary maximum in winter, weak secondary maximum in summer, and two minima occurring during the equinoxes) below $z = 90$ km, while annual variations in GW activities also appear above $z = 90$ km. The long-term (~ 14 years) variability of the observed GW activities is examined by using the deseasonalized and linearly detrended wind variances. The long-term variations of the wind variances are negatively correlated with the 11-year solar cycle above $z = 90$ km, without significant long-term trends below $z = 90$ km.

Potential sources of GWs in the upper mesosphere, including orography, jet stream, and deep convection, are assessed. The steep mountains around KSS can be a source of GWs in autumn and winter, as weak mountain waves can reach the upper mesosphere without encountering a critical level between the surface and the upper mesosphere. The potential of the polar night jet in the upper stratosphere is examined through the residual of nonlinear balance equation (RNBE) at 5 hPa, which is calculated using the ERA-Interim reanalysis data. A large RNBE occurs along the polar vortex in the winter stratosphere, as expected. The correlation coefficient between the observed GWs at $z = 96.8$ km and $|\text{RNBE}|$ poleward of 30°S in winter is relatively smaller than that in spring and autumn due to critical-level filtering and Doppler shifting via strong background wind and wind shear. On the contrary, in spring and autumn, the RNBE near the polar night jet region at 5 hPa correlates well with the observed GW variances at $z = 96.8$ km, implying that the polar night jet is an important source of observed GWs in the upper mesosphere in spring and autumn. Deep convection poleward of 30°S , which is relatively strong in autumn and winter along storm tracks, is found to be one possible source of mesospheric GWs. The CGWMF at 1 hPa in Kang et al. (2018) is the greatest near storm tracks surrounding the Antarctic continent during autumn and winter, with significant positive correlations with GW variances at $z = 96.8$ km in several areas of the storm tracks. GWs generated by deep convection along storm tracks can propagate toward the axis of the polar vortex near KSS in autumn and winter. In addition, secondary GWs generated in the mesosphere is investigated using backward ray-tracing analysis with wave parameters estimated from 8-year (2008–2015) airglow images observed by the all-sky camera at KSS. The secondary GWs mainly occur in winter, likely associated with breaking of orographic GWs that reach the lower mesosphere.

In this study, we have qualitatively investigated the sources of observed GWs in the upper mesosphere based on a correlation analysis. To understand the sources of GWs more precisely, two approaches may be pursued as future research topics. First, the backward ray-tracing analysis should be expanded by using more GW events over KSS, and diagnostic indices for wave sources (such as RNBE for the jet-stream or CGWMF for the deep convection) near each ray-termination position should be investigated. Second, high-resolution numerical simulations that explicitly resolve GWs that are generated by various sources in the lower atmosphere and propagate up into the upper mesosphere should be performed (e.g., Chun & Kim, 2008).

GW activities in the Antarctic MLT regions can vary depending on the observation position due to different wave sources and different background atmosphere. Therefore, a comparison study of GW activities over Antarctica is needed to improve our understanding of wave dynamics and vertical couplings between the lower and upper atmosphere, which will be studied in the future using meteor radar data from various Antarctic stations belonging to the Antarctic Gravity Wave Instrument Network (ANGWIN) (Moffat-Griffin, 2019).

Data Availability Statement

The raw data of the meteor radar and all-sky airglow imager at King Sejong Station are available from Korea Polar Data Center (KPDC) (<https://kpd.c.kopri.re.kr/>). The meteor radar observational data at Rothera station are available at <http://psddb.nerc-bas.ac.uk/data/access/>. The MERRA-2 data set was obtained from https://gmao.gsfc.nasa.gov/reanalysis/MERRA-2/data_access/. The ERA-Interim data are available through <http://apps.ecmwf.int>. The CIRA data are available at <http://data.ceda.ac.uk/badc/cira/data/>. The NCEP CFSR data are available at <https://rda.ucar.edu/datasets/ds093.0/>. The FORTRAN program for the HWM14 data is available at <https://doi.org/10.1002/2014EA000089>.

Acknowledgments

This work was supported by Korea Polar Research Institute (KOPRI, PE19020/PE20100/PE21020). The authors would like to thank to two anonymous reviewers and the editor for their valuable comments and suggestions.

References

- Alexander, M. J. (2015). Global and seasonal variations in three-dimensional gravity wave momentum flux from satellite limb-sounding temperatures. *Geophysical Research Letters*, 42(16), 6860–6867. <https://doi.org/10.1002/2015GL065234>
- Alexander, M. J., Gille, J., Cavanaugh, C., Coffey, M., Craig, C., Eden, T., et al. (2008). Global estimates of gravity wave momentum flux from High Resolution Dynamics Limb Sounder observations. *Journal of Geophysical Research*, 113(D15), D15S18. <https://doi.org/10.1029/2007JD008807>
- Andrews, D. G., Holton, J. R., & Leovy, C. B. (1987). *Middle atmosphere dynamics*. Orlando, FL: Academic press.
- Bacmeister, J. T., & Schoeberl, M. R. (1989). Breakdown of vertically propagating two-dimensional gravity waves forced by orography. *Journal of the Atmospheric Sciences*, 46(14), 2109–2134. [https://doi.org/10.1175/1520-0469\(1989\)046<2109:BOVPTD>2.0.CO;2](https://doi.org/10.1175/1520-0469(1989)046<2109:BOVPTD>2.0.CO;2)
- Baumgaertner, A. J. G., & McDonald, A. J. (2007). A gravity wave climatology for Antarctica compiled from challenging minisatellite payload/global positioning system (CHAMP/GPS) radio occultations. *Journal of Geophysical Research*, 112(5), 1–12. <https://doi.org/10.1029/2006JD007504>
- Beatty, T. J., Hostetler, C. A., & Gardner, C. S. (1992). Lidar observations of gravity waves and their spectra near the mesopause and stratopause at Arecibo. *Journal of the Atmospheric Sciences*, 49, 477–496. [https://doi.org/10.1175/1520-0469\(1992\)049<0477:LOOGWA>2.0.CO;2](https://doi.org/10.1175/1520-0469(1992)049<0477:LOOGWA>2.0.CO;2)
- Becker, E., & Vadas, S. L. (2018). Secondary gravity waves in the winter mesosphere: Results from a high-resolution global circulation model. *Journal of Geophysical Research: Atmospheres*, 123(5), 2605–2627. <https://doi.org/10.1002/2017JD027460>
- Beldon, C. L. (2008). *VHF radar studies of mesosphere and thermosphere* (Doctoral dissertation). Bath, UK: University of Bath. Retrieved from the University of Bath's research portal: <https://researchportal.bath.ac.uk/en/studentTheses/vhf-radar-studies-of-mesosphere-and-thermosphere>
- Beldon, C. L., & Mitchell, N. J. (2009). Gravity waves in the mesopause region observed by meteor radar, 2: Climatologies of gravity waves in the Antarctic and Arctic. *Journal of Atmospheric and Solar-Terrestrial Physics*, 71(8–9), 875–884. <https://doi.org/10.1016/j.jastp.2009.03.009>
- Beldon, C. L., & Mitchell, N. J. (2010). Gravity wave-tidal interactions in the mesosphere and lower thermosphere over Rothera, Antarctica (68°S, 68°W). *Journal of Geophysical Research*, 115(18), 1–12. <https://doi.org/10.1029/2009JD013617>
- Bossert, K., Kruse, C. G., Heale, C. J., Fritts, D. C., Williams, B. P., Snively, J. B., et al. (2017). Secondary gravity wave generation over New Zealand during the DEEPWAVE campaign. *Journal of Geophysical Research: Atmospheres*, 122(15), 7834–7850. <https://doi.org/10.1002/2016JD026079>
- Brown, L. B., Gerrard, A. J., Meriwether, J. W., & Makela, J. J. (2004). All-sky imaging observations of mesospheric fronts in OI 557.7 nm and broadband OH airglow emissions: Analysis of frontal structure, atmospheric background conditions, and potential sourcing mechanisms. *Journal of Geophysical Research*, 109(D19), 1–19. <https://doi.org/10.1029/2003JD004223>
- Chanin, M.-L., & Hauchecorne, A. (1981). Lidar observation of gravity and tidal waves in the stratosphere and mesosphere. *Journal of Geophysical Research*, 86(C10), 9715–9721. <https://doi.org/10.1029/JC086iC10p09715>
- Chen, C., Chu, X., McDonald, A. J., Vadas, S. L., Yu, Z., Fong, W., & Lu, X. (2013). Inertia-gravity waves in Antarctica: A case study using simultaneous lidar and radar measurements at McMurdo/Scott Base (77.8°S, 166.7°E). *Journal of Geophysical Research: Atmospheres*, 118(7), 2794–2808. <https://doi.org/10.1002/jgrd.50318>
- Chen, C., Chu, X., Zhao, J., Roberts, B. R., Yu, Z., Fong, W., et al. (2016). Lidar observations of persistent gravity waves with periods of 3–10 h in the Antarctic middle and upper atmosphere at McMurdo (77.83°S, 166.67°E). *Journal of Geophysical Research: Space Physics*, 121(2), 1483–1502. <https://doi.org/10.1002/2015JA022127>
- Choi, H.-J., & Chun, H.-Y. (2011). Momentum flux spectrum of convective gravity waves. Part I: An update of a parameterization using mesoscale simulations. *Journal of the Atmospheric Sciences*, 68(4), 739–759. <https://doi.org/10.1175/2010JAS3552.1>
- Choi, H.-J., & Chun, H.-Y. (2013). Effects of convective gravity wave drag in the Southern Hemisphere winter stratosphere. *Journal of the Atmospheric Sciences*, 70(7), 2120–2136. <https://doi.org/10.1175/JAS-D-12-0238.1>
- Chu, X., Zhao, J., Lu, X., Harvey, V. L., Jones, R. M., Becker, E., et al. (2018). Lidar observations of stratospheric gravity waves from 2011 to 2015 at McMurdo (77.84°S, 166.69°E), Antarctica: 2. Potential energy densities, lognormal distributions, and seasonal variations. *Journal of Geophysical Research: Atmospheres*, 123(15), 7910–7934. <https://doi.org/10.1029/2017JD027386>
- Chun, H.-Y., & Kim, Y.-H. (2008). Secondary waves generated by breaking of convective gravity waves in the mesosphere and their influence in the wave momentum flux. *Journal of Geophysical Research*, 113, D23107. <https://doi.org/10.1029/2008JD009792>
- Chun, H.-Y., Song, B.-G., Shin, S.-W., & Kim, Y.-H. (2019). Gravity waves associated with jet/front systems. Part I: Diagnostics and their correlations with GWs revealed in high-resolution global analysis data. *Asia-Pacific Journal of Atmospheric Science*, 55(4), 589–608. <https://doi.org/10.1007/s13143-019-00104-1>
- Connor, L. N., & Avery, S. K. (1996). A three-year gravity wave climatology of the mesosphere and lower thermosphere over Kauai. *Journal of Geophysical Research*, 101(D2), 4065–4077. <https://doi.org/10.1029/95JD03065>
- Dee, D. P., Uppala, S. M., Simmons, A. J., Berrisford, P., Poli, P., Kobayashi, S., et al. (2011). The ERA-Interim reanalysis: Configuration and performance of the data assimilation system. *Quarterly Journal of the Royal Meteorological Society*, 137(656), 553–597. <https://doi.org/10.1002/qj.828>
- Dowdy, A. J., Vincent, R. A., Tsutsumi, M., Igarashi, K., Murayama, Y., Singer, W., & Murphy, D. J. (2007). Polar mesosphere and lower thermosphere dynamics: 1. Mean wind and gravity wave climatologies. *Journal of Geophysical Research*, 112(17), 1–16. <https://doi.org/10.1029/2006JD008126>
- Drob, D. P., Emmert, J. T., Crowley, G., Picone, J. M., Shepherd, G. G., Skinner, W., et al. (2008). An empirical model of the Earth's horizontal wind fields: HWM07. *Journal of Geophysical Research*, 113(A12), A12304. <https://doi.org/10.1029/2008JA013668>
- Drob, D. P., Emmert, J. T., Meriwether, J. W., Makela, J. J., Doornbos, E., Conde, M., et al. (2015). An update to the horizontal wind model (HWM): The quiet time thermosphere. *Earth and Space Science*, 2(7), 301–319. <https://doi.org/10.1002/2014EA000089>
- Ern, M., Preusse, P., Alexander, M. J., & Warner, C. D. (2004). Absolute values of gravity wave momentum flux derived from satellite data. *Journal of Geophysical Research*, 109, D20103. <https://doi.org/10.1029/2004JD004752>
- Ern, M., Preusse, P., Gille, J. C., Hepplewhite, C. L., Mlynarczyk, M. G., Russell, J. M., & Riese, M. (2011). Implications for atmospheric dynamics derived from global observations of gravity wave momentum flux in stratosphere and mesosphere. *Journal of Geophysical Research*, 116(19), 1–24. <https://doi.org/10.1029/2011JD015821>
- Fairlie, T. D. A., Fisher, M., & O'Neill, A. (1990). The development of narrow baroclinic zones and other small-scale structure in the stratosphere during simulated major warmings. *Quarterly Journal of Royal Meteorological Society*, 116(492), 287–315. <https://doi.org/10.1002/qj.49711649204>

- Fleming, E. L., Chandra, S., Barnett, J. J., & Corney, M. (1990). Zonal mean temperature, pressure, zonal wind and geopotential height as functions of latitude. *Advances in Space Research*, 10(12), 11–59. [https://doi.org/10.1016/0273-1177\(90\)90386-E](https://doi.org/10.1016/0273-1177(90)90386-E)
- Fritts, D. C., & Alexander, M. J. (2003). Gravity wave dynamics and effects in the middle atmosphere. *Reviews of Geophysics*, 41(1), 1003. <https://doi.org/10.1029/2001RG000106>
- Fritts, D. C., & Nastrom, G. D. (1992). Sources of mesoscale variability of gravity waves. Part II: Frontal, convective, and jet stream excitation. *Journal of the Atmospheric Sciences*, 49(2), 111–127. [https://doi.org/10.1175/1520-0469\(1992\)049<0111:SOMVOG>2.0.CO;2](https://doi.org/10.1175/1520-0469(1992)049<0111:SOMVOG>2.0.CO;2)
- Fritts, D. C., Smith, R. B., Taylor, M. J., Doyle, J. D., Eckermann, S. D., Dörnbrack, A., et al. (2016). The deep propagating gravity wave experiment (DEEPWAVE): An airborne and ground-based exploration of gravity wave propagation and effects from their sources throughout the lower and middle atmosphere. *Bulletin of the American Meteorological Society*, 97(3), 425–453. <https://doi.org/10.1175/BAMS-D-14-00269.1>
- Fritts, D. C., Vadas, S. L., & Yamada, Y. (2002). An estimate of strong local body forcing and gravity wave radiation based on OH airglow and meteor radar observations. *Geophysical Research Letters*, 29(10). <https://doi.org/10.1029/2001GL013753>
- Fritts, D. C., & Vincent, R. A. (1987). Mesospheric Momentum flux studies at Adelaide, Australia: Observations and a gravity wave-tidal interaction model. *Journal of the Atmospheric Sciences*, 44(3), 605–619. [https://doi.org/10.1175/1520-0469\(1987\)044<0605:MMFSAA>2.0.CO;2](https://doi.org/10.1175/1520-0469(1987)044<0605:MMFSAA>2.0.CO;2)
- Fritts, D. C., Wang, L., Taylor, M. J., Pautet, P. D., Criddle, N. R., Kaifler, B., et al. (2019). Large-amplitude mountain waves in the mesosphere observed on 21 June 2014 during DEEPWAVE: 2. Nonlinear dynamics, wave breaking, and instabilities. *Journal of Geophysical Research: Atmospheres*, 124(17–18), 10006–10032. <https://doi.org/10.1029/2019JD030899>
- Fujiwara, M., Wright, J. S., Manney, G. L., Gray, L. J., Anstey, J., Birner, T., et al. (2017). Introduction to the SPARC reanalysis inter-comparison project (S-RIP) and overview of the reanalysis systems. *Atmospheric Chemistry and Physics*, 17(2), 1417–1452. <https://doi.org/10.5194/acp-17-1417-2017>
- Gavrilov, N. M., Fukao, S., & Nakamura, T. (1999). Peculiarities of interannual changes in the mean wind and gravity wave characteristics in the mesosphere over Shigaraki, Japan. *Geophysical Research Letters*, 26(16), 2457–2460. <https://doi.org/10.1029/1999GL900559>
- Gelaro, R., McCarty, W., Suárez, M. J., Todling, R., Molod, A., Takacs, L., et al. (2017). The modern-era retrospective analysis for research and applications, version 2 (MERRA-2). *Journal of Climate*, 30(14), 5419–5454. <https://doi.org/10.1175/JCLI-D-16-0758.1>
- Geller, M. A., Alexander, M. J., Love, P. T., Bacmeister, J., Ern, M., Hertzog, A., et al. (2013). A comparison between gravity wave momentum fluxes in observations and climate models. *Journal of Climate*, 26(17), 6383–6405. <https://doi.org/10.1175/JCLI-D-12-00545.1>
- Heale, C. J., Bossert, K., Vadas, S. L., Hoffmann, L., Dörnbrack, A., Stober, G., et al. (2020). Secondary gravity waves generated by breaking mountain waves over Europe. *Journal of Geophysical Research: Atmospheres*, 125, e2019JD031662. <https://doi.org/10.1029/2019JD031662>
- Hertzog, A., Souprayen, C., & Hauchecorne, A. (2001). Observation and backward trajectory of an inertio-gravity wave in the lower stratosphere. *Annales Geophysicae*, 19(9), 1141–1155. <https://doi.org/10.5194/angeo-19-1141-2001>
- Hindley, N. P., Wright, C. J., Smith, N. D., & Mitchell, N. J. (2015). The southern stratospheric gravity wave hot spot: Individual waves and their momentum fluxes measured by COSMIC GPS-RO. *Atmospheric Chemistry and Physics*, 15(14), 7797–7818. <https://doi.org/10.5194/acp-15-7797-2015>
- Hocking, W. K. (2005). A new approach to momentum flux determinations using SKiYMET meteor radars. *Annales Geophysicae*, 23(7), 2433–2439. <https://doi.org/10.5194/angeo-23-2433-2005>
- Hocking, W. K., & Thayaparan, T. (1997). Simultaneous and colocated observation of winds and tides by MF and meteor radars over London, Canada (43°N, 81°W), during 1994–1996. *Radio Science*, 32(2), 833–865. <https://doi.org/10.1029/96RS03467>
- Isler, J. R., & Fritts, D. C. (1996). Gravity wave variability and interaction with lower-frequency motions in the mesosphere and lower thermosphere over Hawaii. *Journal of the Atmospheric Sciences*, 53(1), 37–48. [https://doi.org/10.1175/1520-0469\(1996\)053<0037:GWVAIW>2.0.CO;2](https://doi.org/10.1175/1520-0469(1996)053<0037:GWVAIW>2.0.CO;2)
- Jacobi, C., Gavrilov, N. M., Kürschner, D., & Fröhlich, K. (2006). Gravity wave climatology and trends in the mesosphere/lower thermosphere region deduced from low-frequency drift measurements 1984–2003 (52.1°N, 13.2°E). *Journal of Atmospheric and Solar-Terrestrial Physics*, 68(17), 1913–1923. <https://doi.org/10.1016/j.jastp.2005.12.007>
- Jia, J. Y., Preusse, P., Ern, M., Chun, H.-Y., Gille, J. C., Eckermann, S. D., & Riese, M. (2014). Sea surface temperature as a proxy for convective gravity wave excitation: A study based on global gravity wave observations in the middle atmosphere. *Annales Geophysicae*, 32(11), 1373–1394. <https://doi.org/10.5194/angeo-32-1373-2014>
- Jiang, J. H., Wu, D. L., & Eckermann, S. D. (2002). Upper Atmosphere Research Satellite (UARS) MLS observation of mountain waves over the Andes. *Journal of Geophysical Research*, 107(D20), 8273. <https://doi.org/10.1029/2002JD002091>
- Kalisch, S., Chun, H.-Y., Ern, M., Preusse, P., Trinh, Q. T., Eckermann, S. D., & Riese, M. (2016). Comparison of simulated and observed convective gravity waves. *Journal of Geophysical Research: Atmospheres*, 121(22), 474–513. <https://doi.org/10.1002/2016JD025235>
- Kalisch, S., Preusse, P., Ern, M., Eckermann, S. D., & Riese, M. (2014). Differences in gravity wave drag between realistic oblique and assumed vertical propagation. *Journal of Geophysical Research: Atmospheres*, 119(17), 10081–10099. <https://doi.org/10.1002/2014JD021779>
- Kam, H., Jee, G., Kim, Y., Ham, Y.-B., & Song, I.-S. (2017). Statistical analysis of mesospheric gravity waves over King Sejong Station, Antarctica (62.2°S, 58.8°W). *Journal of Atmospheric and Solar-Terrestrial Physics*, 155, 86–94. <https://doi.org/10.1016/j.jastp.2017.02.006>
- Kang, M.-J., Chun, H.-Y., & Kim, Y.-H. (2017). Momentum flux of convective gravity waves derived from an offline gravity wave parameterization. Part I: Spatiotemporal variations at source level. *Journal of the Atmospheric Sciences*, 74(10), 3167–3189. <https://doi.org/10.1175/JAS-D-17-0053.1>
- Kang, M.-J., Chun, H.-Y., Kim, Y.-H., Preusse, P., & Ern, M. (2018). Momentum flux of convective gravity waves derived from an offline gravity wave parameterization. Part II: Impacts on the quasi-biennial oscillation. *Journal of the Atmospheric Sciences*, 75(11), 3753–3775. <https://doi.org/10.1175/JAS-D-18-0094.1>
- Kang, M.-J., Chun, H.-Y., & Song, B.-G. (2020). Contributions of convective and orographic gravity waves to the Brewer-Dobson circulation estimated from NCEP CFSR. *Journal of the Atmospheric Sciences*, 77(3), 981–1000. <https://doi.org/10.1175/JAS-D-19-0177.1>
- Ki, M.-O., & Chun, H.-Y. (2011). Inertia gravity waves associated with deep convection observed during the summers of 2005 and 2007 in Korea. *Journal of Geophysical Research*, 116(16), 1–16. <https://doi.org/10.1029/2011JD015684>
- Kim, Y.-H., & Chun, H.-Y. (2009). Effects of the basic-state wind on secondary waves generated by the breaking of gravity waves in the mesosphere. *Asia-Pacific Journal of Atmospheric Sciences*, 45(1), 91–100.
- Kim, Y.-H., Chun, H.-Y., Park, S.-H., Song, I.-S., & Choi, H.-J. (2016). Characteristics of gravity waves generated in the jet-front system in a baroclinic instability simulation. *Atmospheric Chemistry and Physics*, 16(8), 4799–4815. <https://doi.org/10.5194/acp-16-4799-2016>
- Kim, Y.-H., Lee, C.-S., Chung, J.-K., Kim, J.-H., & Chun, H.-Y. (2010). Seasonal Variations of mesospheric gravity waves observed with an airglow all-sky camera at Mt. Bohyun, Korea (36°N). *Journal of Astronomy and Space Sciences*, 27(3), 181–188. <https://doi.org/10.5140/JASS.2010.27.3.181>

- Kim, Y.-J., Eckermann, S. D., & Chun, H.-Y. (2003). An overview of the past, present and future of gravity-wave drag parametrization for numerical climate and weather prediction models. *Atmosphere-Ocean*, 41(1), 65–98. <https://doi.org/10.3137/ao.410105>
- Lee, C., Kim, Y. H., Kim, J.-H., Jee, G., Won, Y.-I., & Wu, D. L. (2013). Seasonal variation of wave activities near the mesopause region observed at King Sejong Station (62.22°S, 58.78°W), Antarctica. *Journal of Atmospheric and Solar-Terrestrial Physics*, 105–106(106), 30–38. <https://doi.org/10.1016/j.jastp.2013.07.006>
- Lindzen, R. S. (1981). Turbulence and stress owing to gravity wave and tidal breakdown. *Journal of Geophysical Research*, 86(C10), 9707–9714. <https://doi.org/10.1029/JC086iC10p09707>
- Liu, A. Z., Lu, X., & Franke, S. J. (2013). Diurnal variation of gravity wave momentum flux and its forcing on the diurnal tide. *Journal of Geophysical Research: Atmospheres*, 118, 1668–1678. <https://doi.org/10.1029/2012JD018653>
- Lomb, N. R. (1976). Least-squares frequency analysis of unequally spaced data. *Astrophysics and Space Science*, 39(2), 447–462. <https://doi.org/10.1007/BF00648343>
- Lu, X., Chen, C., Huang, W., Smith, J. A., Chu, X., Yuan, T., et al. (2015). A coordinated study of 1 h mesoscale gravity waves propagating from Logan to Boulder with CRR L Na Doppler lidars and temperature mapper. *Journal of Geophysical Research: Atmospheres*, 120, 10006–10021. <https://doi.org/10.1002/2015JD023604>
- Lu, X., Chu, X., Fong, W., Chen, C., Yu, Z., Roberts, B. R., & McDonald, A. J. (2015). Vertical evolution of potential energy density and vertical wave number spectrum of Antarctic gravity waves from 35 to 105 km at McMurdo (77.8°S, 166.7°E). *Journal of Geophysical Research: Atmospheres*, 120, 2719–2737. <https://doi.org/10.1002/2014JD022751>
- Lu, X., Chu, X., Li, H., Chen, C., Smith, J. A., & Vadas, S. L. (2017). Statistical characterization of high-to-medium frequency mesoscale gravity waves by lidar-measured vertical winds and temperatures in the MLT. *Journal of Atmospheric and Solar-Terrestrial Physics*, 162, 3–15. <https://doi.org/10.1016/j.jastp.2016.10.009>
- Marks, C. J., & Eckermann, S. D. (1995). A three-dimensional nonhydrostatic ray-tracing model for gravity waves: Formulation and preliminary results for the middle atmosphere. *Journal of the Atmospheric Sciences*, 52(11), 1959–1984. [https://doi.org/10.1175/1520-0469\(1995\)052<1959:ATDNR>2.0.CO;2](https://doi.org/10.1175/1520-0469(1995)052<1959:ATDNR>2.0.CO;2)
- Matsuda, T. S., Nakamura, T., Ejiri, M. K., Tsutsumi, M., Tomikawa, Y., Taylor, M. J., et al. (2017). Characteristics of mesospheric gravity waves over Antarctica observed by Antarctic gravity wave instrument network imagers using 3-D spectral analyses. *Journal of Geophysical Research: Atmospheres*, 122(17), 8969–8981. <https://doi.org/10.1002/2016JD026217>
- Mitchell, N. J., & Beldon, C. L. (2009). Gravity waves in the mesopause region observed by meteor radar: 1. A simple measurement technique. *Journal of Atmospheric and Solar-Terrestrial Physics*, 71(8–9), 866–874. <https://doi.org/10.1016/j.jastp.2009.03.011>
- Mitchell, N. J., Pancheva, D., Middleton, H. R., & Hagan, M. E. (2002). Mean winds and tides in the Arctic mesosphere and lower thermosphere. *Journal of Geophysical Research*, 107(A1). <https://doi.org/10.1029/2001JA900127>
- Moffat-Griffin, T. (2019). An introduction to atmospheric gravity wave science in the polar regions and first results from ANGWIN. *Journal of Geophysical Research: Atmospheres*, 124(3), 1198–1199. <https://doi.org/10.1029/2019JD030247>
- Moffat-Griffin, T., Hibbins, R. E., Jarvis, M. J., & Colwell, S. R. (2011). Seasonal variations of gravity wave activity in the lower stratosphere over an Antarctic Peninsula station. *Journal of Geophysical Research: Atmosphere*, 116(14), 1–10. <https://doi.org/10.1029/2010jd015349>
- Moore, J. T., & Abeling, W. A. (1988). A diagnosis of unbalanced flow in upper levels during the AYE-SESAME I period. *Monthly Weather Review*, 116(12), 2425–2436. [https://doi.org/10.1175/1520-0493\(1988\)116<2425:ADOUFF>2.0.CO;2](https://doi.org/10.1175/1520-0493(1988)116<2425:ADOUFF>2.0.CO;2)
- Murphy, D. J., Alexander, S. P., Klekociuk, A. R., Love, P. T., & Vincent, R. A. (2014). Radiosonde observations of gravity waves in the lower stratosphere over Davis, Antarctica. *Journal of Geophysical Research: Atmospheres*, 119(21), 11973–11996. <https://doi.org/10.1002/2014JD022448>
- Nappo, C. J. (2013). *An introduction to atmospheric gravity waves*. Waltham, MA: Elsevier.
- O’Sullivan, D., & Dunkerton, T. J. (1995). Generation of inertia-gravity waves in a simulated life cycle of baroclinic instability. *Journal of the Atmospheric Sciences*, 52(21), 3695–3716. [https://doi.org/10.1175/1520-0469\(1995\)052<3695:GOIWA>2.0.CO;2](https://doi.org/10.1175/1520-0469(1995)052<3695:GOIWA>2.0.CO;2)
- Park, J., Lühr, H., Lee, C., Kim, Y. H., Jee, G., & Kim, J.-H. (2014). A climatology of medium-scale gravity wave activity in the midlatitude/low-latitude daytime upper thermosphere as observed by CHAMP. *Journal of Geophysical Research: Space Physics*, 119(3), 2187–2196. <https://doi.org/10.1002/2013JA019705>
- Plougonven, R., Hertzog, A., & Guez, L. (2013). Gravity waves over Antarctica and the Southern Ocean: Consistent momentum fluxes in mesoscale simulations and stratospheric balloon observations. *Quarterly Journal of the Royal Meteorological Society*, 139(670), 101–118. <https://doi.org/10.1002/qj.1965>
- Plougonven, R., Hertzog, A., & Teitelbaum, H. (2008). Observations and simulations of a large-amplitude mountain wave breaking over the Antarctic Peninsula. *Journal of Geophysical Research*, 113(16), 1–17. <https://doi.org/10.1029/2007JD009739>
- Plougonven, R., & Snyder, C. (2007). Inertia-gravity waves spontaneously generated by jets and fronts. Part I: Different baroclinic life cycles. *Journal of the Atmospheric Sciences*, 64(7), 2502–2520. <https://doi.org/10.1175/JAS3953.1>
- Plougonven, R., Teitelbaum, H., & Zeitlin, V. (2003). Inertia gravity wave generation by the tropospheric midlatitude jet as given by the fronts and Atlantic storm-track Experiment radio soundings. *Journal of Geophysical Research*, 108(D21), 4686. <https://doi.org/10.1029/2003JD003535>
- Preusse, P., Dörnbrack, A., Eckermann, S. D., Riese, M., Schaeler, B., Bacmeister, J. T., et al. (2002). Space-based measurements of stratospheric mountain waves by CRISTA 1. Sensitivity, analysis method, and a case study. *Journal of Geophysical Research*, 107(D23), 8178. <https://doi.org/10.1029/2001JD000699>
- Preusse, P., Ern, M., Bechtold, P., Eckermann, S. D., Kalisch, S., Trinh, Q. T., & Riese, M. (2014). Characteristics of gravity waves resolved by ECMWF. *Atmospheric Chemistry and Physics*, 14(19), 10483–10508. <https://doi.org/10.5194/acp-14-10483-2014>
- Reeder, M. J., & Griffiths, M. (1996). Stratospheric inertia-gravity waves generated in a numerical model of frontogenesis. II: Wave sources, generation mechanisms and momentum fluxes. *Quarterly Journal of Royal Meteorological Society*, 122(533), 1175–1195. <https://doi.org/10.1002/qj.49712253308>
- Saha, S., Moorthi, S., Pan, H.-L., Wu, X., Wang, J., Nadiga, S., et al. (2010). The NCEP climate forecast system reanalysis. *Bulletin of the American Meteorological Society*, 91(8), 1015–1058. <https://doi.org/10.1175/2010BAMS3001.1>
- Sato, K. (1994). A statistical study of the structure, saturation and sources of inertia-gravity waves in the lower stratosphere observed with the MU radar. *Journal of Atmospheric and Terrestrial Physics*, 56(6), 755–774. [https://doi.org/10.1016/0021-9169\(94\)90131-7](https://doi.org/10.1016/0021-9169(94)90131-7)
- Sato, K., Kumakura, T., & Takahashi, M. (1999). Gravity waves appearing in a high-resolution GCM simulation. *Journal of the Atmospheric Sciences*, 56(8), 1005–1018. [https://doi.org/10.1175/1520-0469\(1999\)056<1005:GWAIAH>2.0.CO;2](https://doi.org/10.1175/1520-0469(1999)056<1005:GWAIAH>2.0.CO;2)
- Sato, K., Watanabe, S., Kawatani, Y., Tomikawa, Y., Miyazaki, K., & Takahashi, M. (2009). On the origins of mesospheric gravity waves. *Geophysical Research Letters*, 36(19), 1–5. <https://doi.org/10.1029/2009GL039908>

- Sato, K., & Yoshiki, M. (2008). Gravity wave generation around the polar vortex in the stratosphere revealed by 3-hourly radiosonde observations at Syowa Station. *Journal of the Atmospheric Sciences*, 65(12), 3719–3735. <https://doi.org/10.1175/2008JAS2539.1>
- Satomura, T., & Sato, K. (1999). Secondary generation of gravity waves associated with the breaking of mountain waves. *Journal of the Atmospheric Sciences*, 56(22), 3847–3858. [https://doi.org/10.1175/1520-0469\(1999\)056<3847:SGOGWA>2.0.CO;2](https://doi.org/10.1175/1520-0469(1999)056<3847:SGOGWA>2.0.CO;2)
- Scargle, J. D. (1982). Studies in astronomical time series analysis. II - Statistical aspects of spectral analysis of unevenly spaced data. *Acta Pathologica Japonica*, 263, 835–853. <https://doi.org/10.1086/160554>
- Schroeder, S., Preusse, P., Ern, M., & Riese, M. (2009). Gravity waves resolved in ECMWF and measured by SABER. *Geophysical Research Letters*, 36, L10805. <https://doi.org/10.1029/2008GL037054>
- Snively, J. B., & Pasko, V. P. (2003). Breaking of thunderstorm-generated gravity waves as a source of short-period ducted waves at mesopause altitudes. *Geophysical Research Letters*, 30(24), 1–4. <https://doi.org/10.1029/2003GL018436>
- Song, I.-S., & Chun, H.-Y. (2005). Momentum flux spectrum of convectively forced internal gravity waves and its application to gravity wave drag parameterization. Part I: Theory. *Journal of the Atmospheric Sciences*, 62(1), 107–124. <https://doi.org/10.1175/JAS-3363.1>
- Song, I.-S., Chun, H. Y., Jee, G., Kim, S. Y., Kim, J., Kim, Y. H., & Taylor, M. A. (2018). Dynamic initialization for whole atmospheric global modeling. *Journal of Advances in Modeling Earth Systems*, 10(9), 2096–2120. <https://doi.org/10.1029/2017MS001213>
- Song, I.-S., Lee, C., Chun, H.-Y., Kim, J.-H., Jee, G., Song, B.-G., & Bacmeister, J. T. (2020). Propagation of gravity waves and its effects on pseudomomentum flux in a sudden stratospheric warming event. *Atmospheric Chemistry and Physics*, 20(12), 7617–7644. <https://doi.org/10.5194/acp-20-7617-2020>
- Song, I.-S., Lee, C., Kim, J.-H., Jee, G., Kim, Y.-H., Choi, H.-J., et al. (2017). Meteor radar observations of vertically propagating low-frequency inertia-gravity waves near the southern polar mesopause region. *Journal of Geophysical Research: Space Physics*, 122(4), 4777–4800. <https://doi.org/10.1002/2016JA022978>
- Tapping, K. F. (2013). The 10.7 cm solar radio flux (F10.7). *Space Weather*, 11(7), 394–406. <https://doi.org/10.1002/swe.20064>
- Taylor, M. J., Pautet, P. D., Fritts, D. C., Kaifler, B., Smith, S. M., Zhao, Y., et al. (2019). Large-amplitude mountain waves in the mesosphere observed on 21 June 2014 during DEEPWAVE: 1. Wave development, scales, momentum fluxes, and environmental sensitivity. *Journal of Geophysical Research: Atmospheres*, 124(19), 10364–10384. <https://doi.org/10.1029/2019jd03089910.1029/2019jd030932>
- Trinh, Q. T., Kalisch, S., Preusse, P., Ern, M., Chun, H.-Y., Eckermann, S. D., et al. (2016). Tuning of a convective gravity wave source scheme based on HIRDLS observations. *Atmospheric Chemistry and Physics*, 16(11), 7335–7356. <https://doi.org/10.5194/acp-16-7335-2016>
- Uccellini, L. W., & Koch, S. E. (1987). The synoptic setting and possible energy sources for mesoscale wave disturbances. *Monthly Weather Review*, 115(3), 721–729. [https://doi.org/10.1175/1520-0493\(1987\)115<0721:TSSAPE>2.0.CO;2](https://doi.org/10.1175/1520-0493(1987)115<0721:TSSAPE>2.0.CO;2)
- Vadas, S. L., & Becker, E. (2018). Numerical modeling of the excitation, propagation, and dissipation of primary and secondary gravity waves during wintertime at McMurdo Station in the Antarctic. *Journal of Geophysical Research: Atmospheres*, 123(17), 9326–9369. <https://doi.org/10.1029/2017JD027974>
- Vadas, S. L., Fritts, D. C., & Alexander, M. J. (2003). Mechanism for the generation of secondary waves in wave breaking regions. *Journal of the Atmospheric Sciences*, 60(1), 194–214. [https://doi.org/10.1175/1520-0469\(2003\)060<0194:MFTGOS>2.0.CO;2](https://doi.org/10.1175/1520-0469(2003)060<0194:MFTGOS>2.0.CO;2)
- Vadas, S. L., Zhao, J., Chu, X., & Becker, E. (2018). The excitation of secondary gravity waves from local body forces: Theory and observation. *Journal of Geophysical Research: Atmospheres*, 123(17), 9296–9325. <https://doi.org/10.1029/2017JD027970>
- Vincent, R. A. (1984). MF/HF radar measurements of the dynamics of the mesopause region-A review. *Journal of Atmospheric and Terrestrial Physics*, 46(11), 961–974. [https://doi.org/10.1016/0021-9169\(84\)90003-5](https://doi.org/10.1016/0021-9169(84)90003-5)
- Vincent, R. A. (1994). Gravity-wave motions in the mesosphere and lower thermosphere observed at Mawson, Antarctica. *Journal of Atmospheric and Terrestrial Physics*, 56(5), 593–602. [https://doi.org/10.1016/0021-9169\(94\)90100-7](https://doi.org/10.1016/0021-9169(94)90100-7)
- Vincent, R. A., & Fritts, D. C. (1987). A climatology of gravity wave motions in the mesopause region at Adelaide, Australia. *Journal of the Atmospheric Sciences*, 44(4), 748–760. [https://doi.org/10.1175/1520-0469\(1987\)044<0748:ACOGWM>2.0.CO;2](https://doi.org/10.1175/1520-0469(1987)044<0748:ACOGWM>2.0.CO;2)
- Vincent, R. A., & Reid, I. M. (1983). HF doppler measurements of mesospheric gravity wave momentum fluxes. *Journal of the Atmospheric Sciences*, 40(5), 1321–1333. [https://doi.org/10.1175/1520-0469\(1983\)040<1321:HDMOMG>2.0.CO;2](https://doi.org/10.1175/1520-0469(1983)040<1321:HDMOMG>2.0.CO;2)
- Wang, S., & Zhang, F. (2007). Sensitivity of mesoscale gravity waves to the baroclinicity of jet-front systems. *Monthly Weather Review*, 135(2), 670–688. <https://doi.org/10.1175/mwr3314.1>
- Whiteway, J. A., Duck, T. J., Donovan, D. P., Bird, J. C., Pal, S. R., & Carswell, A. I. (1997). Measurements of gravity wave activity within and around the Arctic stratospheric vortex. *Geophysical Research Letters*, 24(11), 1387–1390. <https://doi.org/10.1029/97GL01322>
- Wilks, D. S. (2011). *Statistical methods in the atmospheric sciences*. Boston, MA: Elsevier.
- Wilson, R., Chanin, M. L., & Hauchecorne, A. (1991). Gravity waves in the middle atmosphere observed by Rayleigh lidar: 2. Climatology. *Journal of Geophysical Research*, 96(D3), 5169–5183. <https://doi.org/10.1029/90JD02610>
- Wrasse, C. M., Nakamura, T., Tsuda, T., Takahashi, H., Medeiros, A. F., Taylor, M. J., et al. (2006). Reverse ray tracing of the mesospheric gravity waves observed at 23°S (Brazil) and 7°S (Indonesia) in airlow imagers. *Journal of Atmospheric and Solar-Terrestrial Physics*, 68(2), 163–181. <https://doi.org/10.1016/j.jastp.2005.10.012>
- Wu, D. L., & Zhang, F. (2004). A study of mesoscale gravity waves over the North Atlantic with satellite observations and a mesoscale model. *Journal of Geophysical Research*, 109(D22), D22104. <https://doi.org/10.1029/2004JD005090>
- Yamanaka, M. D., Fukao, S., Matsumoto, H., Sato, T., Tsuda, T., & Kato, S. (1989). Internal gravity wave selection in the upper troposphere and lower stratosphere observed by the MU radar: Preliminary results. *Pure and Applied Geophysics*, 130(2–3), 481–495. https://doi.org/10.1007/BF0087447010.1007/978-3-0348-5825-0_20
- Yamashita, C., Chu, X., Liu, H.-L., Espy, P. J., Nott, G. J., & Huang, W. (2009). Stratospheric gravity wave characteristics and seasonal variations observed by lidar at the South Pole and Rothera, Antarctica. *Journal of Geophysical Research*, 114(12), 1–11. <https://doi.org/10.1029/2008JD011472>
- Yoo, J. H., Choi, T., Chun, H. Y., Kim, Y. H., Song, I. S., & Song, B. G. (2018). Inertia-gravity waves revealed in radiosonde data at Jang Bogo Station, Antarctica (74°37'S, 164°13'E): 1. Characteristics, energy, and momentum flux. *Journal of Geophysical Research: Atmospheres*, 123, 13305–13331. <https://doi.org/10.1029/2018JD029164>
- Yoo, J. H., Song, I. S., Chun, H. Y., & Song, B. G. (2020). Inertia-gravity waves revealed in radiosonde data at Jang Bogo Station, Antarctica (74°37'S, 164°13'E): 2. Potential sources and their relation to inertia-gravity waves. *Journal of Geophysical Research: Atmospheres*, 125(7), 1–31. <https://doi.org/10.1029/2019JD032260>
- Yoshiki, M., Kizu, N., & Sato, K. (2004). Energy enhancements of gravity waves in the Antarctic lower stratosphere associated with variations in the polar vortex and tropospheric disturbances. *Journal of Geophysical Research*, 109(D23), 1–12. <https://doi.org/10.1029/2004JD004870>
- Yoshiki, M., & Sato, K. (2000). A statistical study of gravity waves in the polar regions based on operational radiosonde data. *Journal of Geophysical Research*, 105(D14), 17995–18011. <https://doi.org/10.1029/2000JD002024>

- Zhang, F. (2004). Generation of mesoscale gravity waves in upper-tropospheric jet-front systems. *Journal of the Atmospheric Sciences*, 61(4), 440–457. [https://doi.org/10.1175/1520-0469\(2004\)061<0440:GOMGWI>2.0.CO;2](https://doi.org/10.1175/1520-0469(2004)061<0440:GOMGWI>2.0.CO;2)
- Zhang, F., Davis, C. A., Kaplan, M. L., & Koch, S. E. (2001). Wavelet analysis and the governing dynamics of a large-amplitude mesoscale gravity-wave event along the East Coast of the United States. *Quarterly Journal of Royal Meteorological Society*, 127(577), 2209–2245. <https://doi.org/10.1002/qj.49712757702>
- Zhang, F., Koch, S. E., Davis, C. A., & Kaplan, M. L. (2000). A survey of unbalanced flow diagnostics and their application. *Advances in Atmospheric Sciences*, 17(2), 165–183. <https://doi.org/10.1007/s00376-000-0001-1>
- Zhao, J., Chu, X., Chen, C., Lu, X., Fong, W., Yu, Z., et al. (2017). Lidar observations of stratospheric gravity waves from 2011 to 2015 at McMurdo (77.84°S, 166.69°E), Antarctica: 1. Vertical wavelengths, periods, and frequency and vertical wave number spectra. *Journal of Geophysical Research: Atmospheres*, 122(10), 5041–5062. <https://doi.org/10.1002/2016JD026368>